WILEY | Hindawi

Research Article

Hyper Coupled Map Lattices for Hiding Multiple Images

Rasa Smidtaite [ID],[1] Jurate Ragulskiene,[2] Liepa Bikulciene [ID],[1] and Minvydas Ragulskis [ID][2]

[1]*Department of Applied Mathematics, Kaunas University of Technology, Studentu 50-429, Kaunas 51368, Lithuania*
[2]*Department of Mathematical Modelling, Kaunas University of Technology, Studentu 50-146, Kaunas 51368, Lithuania*

Correspondence should be addressed to Rasa Smidtaite; rasa.smidtaite@ktu.lt and Minvydas Ragulskis; minvydas.ragulskis@ktu.lt

The concept of a hyper coupled map lattice (CML) is presented in this paper. The complexity of the lattice is increased not by adding another spatial dimension of the lattice but by replacing scalar nodal variables by multidimensional square matrices of iterative variables. The proposed scheme exploits the nonlinear effects of the spatiotemporal divergence induced by nilpotent nodal matrices to generate separate secret images at different discrete moments of time during the evolution of the CML. The time variable plays the primary role in the decoding stage of the scheme. The carrying capacity of the proposed scheme is $n-1$ different dichotomous digital images, where n is the dimension of the nilpotent nodal matrices. Computational experiments are used to demonstrate the efficacy of the proposed scheme.

1. Introduction

Coupled map lattice (CML) is a classical spatiotemporal chaotic system with complex dynamic behavior. CML was formally proposed by Kaneko in 1984 [1–3], where each node is coupled with its closest neighbors. Since then, many types of coupling were introduced [4–13]. A one-way coupling map lattice is used to derive a cryptosystem key generator in [4]. A nonadjacent coupled map lattice, where connected nodes are dynamically determined through a nonlinear Arnold cat map, is applied to diffuse color channels in image DNA encryption algorithm in [5]. Nonlinear (mixed adjacent and nonadjacent) coupled map lattices enabled an image encryption algorithm with simultaneous permutation and diffusion process [6, 7]. Dynamically coupled map lattices are based on the idea to use chaotic map or other function as the coupling coefficient in order to ensure the changing degree of the coupling between lattices [8]. A pseudorandom coupled map lattices system with perturbation is proposed in [9]. Wang et al. [10] proposed a new scrambling method based on customized globally CML including a superposition of four chaotic maps as a coupling term. The scheme of pseudorandom number generator combines the improved CML and time-varying

delay in [11]. CML extensions when a scalar variable is replaced by a square matrix of variables are introduced in [12, 13].

Images play a significant role in many applications including personal use, commerce, medicine, and the military [14]. These images often contain confidential and sensitive information that needs to be protected from unauthorized access [15]. Technology advances lead to a phenomenal increase in virtual communication and information interchange. Therefore, image security became an inescapable problem of high importance in different areas [16]. The confidentiality of digital image can be maintained by data encryption [17, 18]. A variety of techniques for encrypting images include cryptography [19, 20], watermarking [21, 22], and steganography [23, 24].

Various coverless steganography methods are reviewed in [25], along with a survey of fundamental approaches based on hashing techniques, mapping relations, and feature extraction. A coverless image steganography framework is proposed in [26], where appropriate original images already containing the secret data are chosen from a constructed database and are used as stego images, which makes it robust against steganalysis. The steganography without embedding technique based on generative adversarial networks is

introduced in [27], where the generated cover images themselves are stego images carrying secret information. A coverless information hiding method where a secret image is embedded into a public image and then the obtained synthetic image is used as an input to the hiding method based on a generative model is investigated in [28]. Hiding capacity, success rate, and security are improved by the suggested coverless information hiding technique based on the retrieval of the massive amount of web text on the Internet using a web spider technology [29].

The potential for the exploitation of chaos in cryptography and steganography has gained interest in the past few decades [30–33]. Since the pioneering work on chaos-based image encryption by Fridrich in 1997 [30], many information encryption schemes have been proposed based on continuous time [31, 32], discrete time [34, 35], and fractional [36, 37] chaotic systems. Image encryption techniques based on discrete chaotic maps are more often used due to simple structure and faster operational speed [38]. The main idea of a discrete chaos-based image encryption algorithm is based on the system's ability to produce pseudorandom numbers; therefore, the selection of a proper chaotic map is a primary task in any image hiding application [33]. Several chaotic maps have been employed in the algorithms of image encryption including the logistic map [39–41], tent map [42, 43], Arnold map [44, 45], circle map [46], Henon map [47, 48], and Baker map [49, 50].

Image encryption schemes based on coupled map lattices (CML) have attracted the attention of many researchers, as spatiotemporal chaotic systems do possess the advantages of more complex dynamical behavior and lower computational overhead compared to a single chaotic map [51]. An image encryption scheme with the permutation diffusion mechanism based on 1D CML with a local map defined as a nonlinear chaotic algorithm is proposed in [52]. The cipher based on 2D chaotic lattices is presented in [53], where lattices are used both to generate pseudorandom sequences and encrypt image blocks one by one. Logistic, sine, and tent maps are mixed into one CML in order to provide a more secure scheme to encrypt image [54]. A novel image encryption scheme employing a pseudorandom coupled map lattices model based on hybrid elementary cellular automata and the Chirikov standard map is presented in [9]. The effect of temporary divergence in a CML of nilpotent matrices of order 2 is exploited for the construction of an image hiding scheme in [55, 56].

Beside schemes suitable to hide a single image, multi-image hiding methods have also been proposed. A multiple image hiding framework based on joint compressive autoencoders when is provided in [57]. A technique for hiding multi-images in an image using the least significant bit algorithm and Arnold transformation is presented in [58]. An invertible neural network is used in the multiple images hiding framework [59]. A multilayered embedded technique, where images are first unified to one and then the composited image is encrypted in the pattern of diffusion-scrambling-nonlinear transform is proposed in [60]. It can be noted that all these techniques aim to hide multiple secret images into a single cover image. All these techniques use different transformations of the single cover image. The main difference of the proposed scheme from the mentioned methods is based on the spatiotemporal properties of the introduced CML. In other words, the proposed scheme exploits the nonlinear effects of spatiotemporal divergence exhibited by a special type of CML used to generate separate secret images at different discrete moments of time during the evolution of the CML. This is the main advantage of the proposed scheme in regards to the previously discussed methods, as the time variable now plays the primary role in the decoding stage of the scheme.

The main purpose of this study is to employ a single coupled map lattice of higher-order nilpotent matrices and their properties of temporary divergence in order to hide multiple secret images without unifying those images into a single cover image. A new type of multiple images hiding scheme in a coupled map lattice of nilpotent matrices is developed for these purposes. The paper is structured as follows. An overview of the dynamics of a single iterative map of matrices as well as the dynamics of the two-dimensional lattice of matrices is discussed in Sections 2. The concept and the properties of the hyper CML are introduced and discussed in Section 3. The encoding scheme of multiple images and supporting computational experiments are provided in Section 4. Concluding remarks are given in the last section.

2. Preliminaries

2.1. The Iterative Map of Matrices of Order 2. Let us consider a scalar iterative map

$$x^{(t+1)} = f\left(x^{(t)}\right), \quad t = 0, 1, 2, \ldots, \tag{1}$$

where $x^{(0)} \in \mathbb{R}$ is the initial condition and the mapping function f can be expanded into a formal power series:

$$f(z) = \sum_{k=0}^{\infty} c_k \frac{z^k}{k!}, \tag{2}$$

where $z \in \mathbb{R}$, $c_k \in \mathbb{R}$. The scalar variable $x^{(t)}$ in (1) can be replaced by a second-order square matrix of variables $\mathbf{X}^{(t)} = \begin{bmatrix} x_{11}^{(t)} & x_{12}^{(t)} \\ x_{21}^{(t)} & x_{22}^{(t)} \end{bmatrix}$, where each element of the matrix is a separate scalar variable: $x_{11}^{(t)}, x_{12}^{(t)}, x_{21}^{(t)} x_{22}^{(t)} \in \mathbb{R}$ [61, 62]. Then, the iterative map of matrices reads

$$\mathbf{X}^{(t+1)} = f\left(\mathbf{X}^{(t)}\right), \quad t = 0, 1, 2, \ldots. \tag{3}$$

It appears that the dynamics of such an iterative map of matrices depends on the matrix of initial conditions $\mathbf{X}^{(0)}$ [61, 62]. If the eigenvalues of $\mathbf{X}^{(0)}$ are different ($\lambda_1^{(0)} \neq \lambda_2^{(0)}$), then the matrix of initial conditions can be expressed in the form of an idempotent matrix:

$$\mathbf{X}^{(0)} = \lambda_1^{(0)} \mathbf{D}_1 + \lambda_2^{(0)} \mathbf{D}_2, \tag{4}$$

where $\mathbf{D}_1$ and $\mathbf{D}_2$ are conjugate idempotents. The following properties do hold for conjugate idempotents: $\det(\mathbf{D}_1) = \det(\mathbf{D}_2) = 0$; $\mathbf{D}_1 + \mathbf{D}_2 = \mathbf{I}$; $\mathbf{D}_1\mathbf{D}_1 = \mathbf{D}_1$; $\mathbf{D}_2\mathbf{D}_2 = \mathbf{D}_2$;

$\mathbf{D}_1\mathbf{D}_2 = \mathbf{D}_2\mathbf{D}_1 = \boldsymbol{\Theta}$, where $\mathbf{I}$ and $\boldsymbol{\Theta}$ are the second-order identity and zero matrices.

The evolution of (3) starting with an idempotent 2×2 matrix results into two scalar iterative maps of the eigenvalues [62]:

$$\begin{cases} \lambda_1^{(t+1)} = f\big(\lambda_1^{(t)}\big), \\ \lambda_2^{(t+1)} = f\big(\lambda_2^{(t)}\big), \end{cases} \quad t = 0, 1, 2, \ldots. \tag{5}$$

However, if the eigenvalues of $\mathbf{X}^{(0)}$ do coincide $(\lambda_1^{(0)} = \lambda_2^{(0)} = \lambda_0^{(0)})$, then the matrix of initial conditions can be expressed in the form of a nilpotent matrix:

$$\mathbf{X}^{(0)} = \lambda_0^{(0)}\mathbf{I} + \mu_1^{(0)}\mathbf{N}, \tag{6}$$

where $\mu_1^{(0)}$ is an auxiliary parameter; $\mathbf{N}$ is a nilpotent. The following properties do hold for a nilpotent: $\mathbf{N}^2 = \boldsymbol{\Theta}$; $\det(\mathbf{N}) = 0$. If the matrix of initial conditions $\mathbf{X}^{(0)}$ is a nilpotent matrix, then the matrices produced by the iterative map are also nilpotent matrices:

$$\begin{aligned}
\mathbf{X}^{(t+1)} = f\big(\mathbf{X}^{(t)}\big) &= \sum_{k=0}^{\infty} \frac{c_k}{k!}\big(\mathbf{X}^{(t)}\big)^k = \sum_{k=0}^{\infty} \frac{c_k}{k!}\big(\lambda_0^{(t)}\mathbf{I} + \mu_1^{(t)}\mathbf{N}\big)^k \\
&= \sum_{k=0}^{\infty} \frac{c_k}{k!}\left(\binom{k}{0}\big(\lambda_0^{(t)}\big)^k\mathbf{I}^k + \binom{k}{1}\big(\lambda_0^{(t)}\big)^{k-1}\mu_1^{(t)}\mathbf{I}^{k-1}\mathbf{N}\right. \\
&\quad \left. + \binom{k}{2}\big(\lambda_0^{(t)}\big)^{k-2}\big(\mu_1^{(t)}\big)^2\mathbf{I}^{k-2}\mathbf{N}^2 + \cdots + \binom{k}{k}\big(\mu_1^{(t)}\big)^k\mathbf{N}^k\right) \\
&= \sum_{k=0}^{\infty} \frac{c_k}{k!}\left(\big(\lambda_0^{(t)}\big)^k\mathbf{I} + k\big(\lambda_0^{(t)}\big)^{k-1}\mu_1^{(t)}\mathbf{N}\right) \\
&= \left(\sum_{k=0}^{\infty} \frac{c_k}{k!}\big(\lambda_0^{(t)}\big)^k\right)\mathbf{I} + \left(\sum_{k=0}^{\infty} \frac{c_k}{k!}k\big(\lambda_0^{(t)}\big)^{k-1}\right)\mu_1^{(t)}\mathbf{N} \\
&= f\big(\lambda_0^{(t)}\big)\mathbf{I} + \mu_1^{(t)}f'\big(\lambda_0^{(t)}\big)\mathbf{N},
\end{aligned} \tag{7}$$

where $t = 0, 1, \ldots$, $\mu_1^{(0)} \neq 0$; $\binom{k}{p} = k!/(p!(k-p)!)$ is a binomial coefficient; $f'\big(\lambda_0^{(t)}\big)$ denotes the derivative of f computed at $\lambda_0^{(t)}$ [61]. Therefore, the model (3) initialized with a nilpotent 2×2 matrix results into two intertwined scalar iterative maps [61, 62]:

$$\begin{cases} \lambda_0^{(t+1)} = f\big(\lambda_0^{(t)}\big), \\ \mu_1^{(t+1)} = \mu_1^{(t)}f'\big(\lambda_0^{(t)}\big), \end{cases} \quad t = 0, 1, 2, \ldots; \mu_1^{(0)} \neq 0, \tag{8}$$

where the initial condition of the scalar map of eigenvalues is $\lambda_0^{(0)}$. Note that the second scalar iterative map in (8) defines the evolution of the auxiliary parameter $\mu_1^{(t)}$ where the derivative of the mapping function is computed at $\lambda_0^{(t)}$.

The effect of the explosive divergence of $\mu_1^{(t)}$ is observed when the Lyapunov exponent of the original scalar iterative map (1) becomes positive [62].

2.2. The Coupled Map Lattice of the Second-Order Nilpotent Matrices.
Let us consider the classical two-dimensional CML model [3] defined on a square lattice $[1, N_x] \times [1, N_y]$:

$$\begin{aligned}
x^{(t+1)}(i, j) &= (1 - \varepsilon)f\big(x^{(t)}(i, j)\big) \\
&\quad + \frac{\varepsilon}{4}\big(f\big(x^{(t)}(i+1, j)\big) + f\big(x^{(t)}(i-1, j)\big) \\
&\quad + f\big(x^{(t)}(i, j+1)\big) + f\big(x^{(t)}(i, j-1)\big)\big),
\end{aligned} \tag{9}$$

where $t = 0, 1, 2, \ldots$; $x^{(t)}(i, j)$ is the discrete state variable; indices (i, j) denote the position of the node $(i = 1, 2, \ldots, N_x, j = 1, 2, \ldots, N_y)$; f is the scalar mapping function; ε is the coupling parameter $(0 \leq \varepsilon \leq 1)$.

The scalar nodal variable $x^{(t)}(i, j)$ in (9) can be replaced by the square matrix $\mathbf{X}^{(t)}(i, j) \in \mathbb{R}^{2 \times 2}$. Such a replacement results into a CML of matrices [55]. It appears that the

dynamics of CML of matrices also depends on the type of the matrix of initial conditions [55]. Now, the dynamics of CML of 2×2 nilpotent matrices is governed by the following iterative model [55]:

$$
\begin{cases}
\lambda_0^{(t+1)}(i, j) = f\left(\lambda_0^{(t)}(i, j)\right), \\[2mm]
\mu_1^{(t+1)}(i, j) = (1 - \varepsilon)\mu_1^{(t)}(i, j)f^{'}\left(\lambda_0^{(t)}(i, j)\right) \\[2mm]
+\dfrac{\varepsilon}{4}\left(\mu_1^{(t)}(i+1, j)f^{'}\left(\lambda_0^{(t)}(i+1, j)\right)\right. \\[2mm]
+\mu_1^{(t)}(i-1, j)f^{'}\left(\lambda_0^{(t)}(i-1, j)\right) \\[2mm]
+\mu_1^{(t)}(i, j+1)f^{'}\left(\lambda_0^{(t)}(i, j+1)\right) \\[2mm]
+\mu_1^{(t)}(i, j-1)f^{'}\left(\lambda_0^{(t)}(i, j-1)\right)\right),
\end{cases}
\tag{10}
$$

where $\mu_1^{(0)}(i, j)$ is the nodal auxiliary parameter; $\lambda_0^{(0)}(i, j)$ is the recurrent eigenvalue of the matrix of initial conditions at the node (i, j).

2.3. Image Hiding Scheme in a CML of Two-Dimensional Matrices.

The effect of temporary divergence in a CML of two-dimensional matrices enables to construct the image hiding scheme which does not require a different image for the retrieval of the secret image [55]. The CML of two-dimensional matrices is perturbed at the nodes corresponding to the dot skeleton representation of the secret image [55].

The evolution of patterns produced by the CML of two-dimensional matrices yield the secret image. The number of time-forward iterations required to produce the pattern closest to the original secret image is one of the parameters of the image-hiding scheme presented in [55].

2.4. Iterative Map of Matrices of Order n.

The natural extension of the iterative map of 2×2 matrices discussed in Section 2.1 is based on the larger dimension of the matrix. The scalar variable $x^{(t)}$ in (1) can be replaced by a square matrix of order n [56].

It appears that the dynamics of the iterative map of matrices of order n is much more complex if compared to the iterative map of matrices of order 2 [56]. The number of different scenarios is now predetermined by the current packing code which defines the recurrence indices of eigenvalues of the matrix of initial conditions [56]. In analogy to the iterative map of matrices of order 2, the iterative map of order n splits into n independent scalar iterative maps of eigenvalues if only all eigenvalues are different (this situation corresponds to the smallest possible packing code). On the

opposite, when all eigenvalues of the matrix of initial conditions do coincide (this situation corresponds to the largest possible packing code), the effect of divergence of the iterative map of matrices of order n is governed by $n - 1$ auxiliary parameters $\mu_1, \mu_2, \ldots, \mu_{n-1}$ [56]:

$$
\begin{cases}
\lambda_0^{(t+1)} = f\left(\lambda_0^{(t)}\right), \\[2mm]
\mu_1^{(t+1)} = \mu_1^{(t)}f^{'}\left(\lambda_0^{(t)}\right), \\[2mm]
\mu_2^{(t+1)} = \mu_2^{(t)}f^{'}\left(\lambda_0^{(t)}\right) + \dfrac{\left(\mu_1^{(t)}\right)^2}{2!}f^{''}\left(\lambda_0^{(t)}\right), \\[3mm]
\mu_3^{(t+1)} = \mu_3^{(t)}f^{'}\left(\lambda_0^{(t)}\right) + \dfrac{2\mu_1^{(t)}\mu_2^{(t)}}{2!}f^{''}\left(\lambda_0^{(t)}\right) + \dfrac{\left(\mu_1^{(t)}\right)^3}{3!}f^{'''}\left(\lambda_0^{(t)}\right), \\[3mm]
\mu_4^{(t+1)} = \mu_4^{(t)}f^{'}\left(\lambda_0^{(t)}\right) + \dfrac{2\mu_1^{(t)}\mu_3^{(t)} + \left(\mu_2^{(t)}\right)^2}{2!}f^{''}\left(\lambda_0^{(t)}\right) \\[3mm]
+ \dfrac{3\left(\mu_1^{(t)}\right)^2\mu_2^{(t)}}{3!}f^{'''}\left(\lambda_0^{(t)}\right) + \dfrac{\left(\mu_1^{(t)}\right)^4}{4!}f^{iv}\left(\lambda_0^{(t)}\right), \\[3mm]
\ldots \\[2mm]
\mu_{n-1}^{(t+1)} = \mu_{n-1}^{(t)}f^{'}\left(\lambda_0^{(t)}\right) + \dfrac{\sum_{i_1=1}^{n-2}\mu_{i_1}^{(t)}\mu_{n-1-i_1}^{(t)}}{2!}f^{''}\left(\lambda_0^{(t)}\right) \\[3mm]
+ \dfrac{\sum_{1 \le i_1, i_2, i_3 \le n-3}^{i_1+i_2+i_3=n-1}\mu_{i_1}^{(t)}\mu_{i_2}^{(t)}\mu_{i_3}^{(t)}}{3!}f^{'''}\left(\lambda_0^{(t)}\right) \\[3mm]
+ \cdots + \dfrac{\left(\mu_1^{(t)}\right)^{n-1}}{(n-1)!}f^{(n-1)}\left(\lambda_0^{(t)}\right),
\end{cases}
\tag{11}
$$

where $\mu_l^{(0)}$ and $l = 1, 2, \ldots, n - 1$ are auxiliary parameters, and $f^{(s)}$ denotes the s order derivative of the mapping function f.

3. The Governing Equations for a Hyper CML

Let us consider a 2D CML of scalar maps where each discrete node is coupled with its four closest neighbors on a rectangular domain $[1, N_x] \times [1, N_y]$. Let us replace each scalar nodal variable by a n-dimensional square matrix of discrete variables.

Definition 1. Hyper CML is a 2D CML such that as follows:

(1) Each scalar discrete node is replaced by an n-dimensional square matrix of discrete variables

(2) The size of the matrix n is the same for each node

(3) The divergence code for each nodal matrix is $[0\ 1\ 2\ \ldots\ (n - 2)(n - 1)]$

(4) The nilpotent of each nodal matrix is the same (note that this condition does not require the recurrent eigenvalue of the nodal matrix to be the same at each node).

Corollary 2. *If a CML is a hyper CML at $t = 0$, then the CML will remain a hyper CML in every discrete time-forward step $t = 1, 2, \ldots$.*

Proof. The proof follows directly from the structure of the CML lattice and equation (11). □

Example 1. Let us consider a hyper CML at iteration t. Without loss of generality, let us consider the node (i, j) and its four neighbors only. Also, let us consider that the dimension of nodal matrices is 2×2. All five nodal nilpotent are set to $\mathbf{N} = \begin{bmatrix} -0.3 & 0.9 \\ -0.1 & 0.3 \end{bmatrix}$.

The nodal mapping function f is set at the logistic mapping function: $x^{(t+1)} = 3.6 x^{(t)} (1 - x^{(t)})$. The coupling parameter ε is set to 0.1. Then, a single time-forward iteration produces new nodal matrices (according to equation (12)). However, the offspring CML is still a hyper CML because all five nodal nilpotent remain unchanged (Table 1).

The governing equations of a hyper CML follow from the algebraic structure of the iterative nilpotent matrices with the largest divergence code:

$$\lambda_0^{(t+1)}(i, j) = f\left(\lambda_0^{(t)}(i, j)\right),$$

$$\mu_1^{(t+1)}(i, j) = (1 - \varepsilon)\mu_1^{(t)}(i, j)f'\left(\lambda_0^{(t)}(i, j)\right)$$

$$+ \frac{\varepsilon}{4}\left(\mu_1^{(t)}(i + 1, j)f'\left(\lambda_0^{(t)}(i + 1, j)\right)\right.$$

$$+ \mu_1^{(t)}(i - 1, j)f'\left(\lambda_0^{(t)}(i - 1, j)\right)$$

$$+ \mu_1^{(t)}(i, j + 1)f'\left(\lambda_0^{(t)}(i, j + 1)\right)$$

$$+ \left.\mu_1^{(t)}(i, j - 1)f'\left(\lambda_0^{(t)}(i, j - 1)\right)\right),$$

$$\mu_2^{(t+1)}(i, j) = (1 - \varepsilon)\left(\mu_2^{(t)}(i, j)f'\left(\lambda_0^{(t)}(i, j)\right) + \frac{\left(\mu_1^{(t)}(i, j)\right)^2}{2!}f''\left(\lambda_0^{(t)}(i, j)\right)\right)$$

$$+ \frac{\varepsilon}{4}\left(\mu_2^{(t)}(i + 1, j)f'\left(\lambda_0^{(t)}(i + 1, j)\right) + \frac{\left(\mu_1^{(t)}(i + 1, j)\right)^2}{2!}f''\left(\lambda_0^{(t)}(i + 1, j)\right)\right.$$

$$+ \mu_2^{(t)}(i - 1, j)f'\left(\lambda_0^{(t)}(i - 1, j)\right) + \frac{\left(\mu_1^{(t)}(i - 1, j)\right)^2}{2!}f''\left(\lambda_0^{(t)}(i - 1, j)\right)$$

$$+ \mu_2^{(t)}(i, j + 1)f'\left(\lambda_0^{(t)}(i, j + 1)\right) + \frac{\left(\mu_1^{(t)}(i, j + 1)\right)^2}{2!}f''\left(\lambda_0^{(t)}(i, j + 1)\right)$$

$$+ \left.\mu_2^{(t)}(i, j - 1)f'\left(\lambda_0^{(t)}(i, j - 1)\right) + \frac{\left(\mu_1^{(t)}(i, j - 1)\right)^2}{2!}f''\left(\lambda_0^{(t)}(i, j - 1)\right)\right),$$

$$\ldots$$

$$\mu_{n-1}^{(t+1)}(i, j) = (1 - \varepsilon)\left(\mu_{n-1}^{(t)}(i, j)f'\left(\lambda_0^{(t)}(i, j)\right)\right.$$

$$+ \frac{\sum_{i_1=1}^{n-2}\mu_{i_1}^{(t)}(i, j)\mu_{n-1-i_1}^{(t)}(i, j)}{2!}f''\left(\lambda_0^{(t)}(i, j)\right)$$

$$+ \frac{\sum_{1 \le i_1, i_2, i_3 \le n-3}^{i_1+i_2+i_3=n-1} \mu_{i_1}^{(t)}(i,j) \mu_{i_2}^{(t)}(i,j) \mu_{i_3}^{(t)}(i,j)}{3!} f''\left(\lambda_0^{(t)}(i,j)\right)$$

$$+ \cdots + \frac{\left(\mu_1^{(t)}(i,j)\right)^{n-1}}{(n-1)!} f^{(n-1)}\left(\lambda_0^{(t)}(i,j)\right) \Bigg)$$

$$\frac{\varepsilon}{4}\Bigg(\mu_{n-1}^{(t)}(i+1,j) f'\left(\lambda_0^{(t)}(i+1,j)\right)$$

$$+ \frac{\sum_{i_1=1}^{n-2} \mu_{i_1}^{(t)}(i+1,j) \mu_{n-1-i_1}^{(t)}(i+1,j)}{2!} f''\left(\lambda_0^{(t)}(i+1,j)\right)$$

$$+ \frac{\sum_{1 \le i_1, i_2, i_3 \le n-3}^{i_1+i_2+i_3=n-1} \mu_{i_1}^{(t)}(i+1,j) \mu_{i_2}^{(t)}(i+1,j) \mu_{i_3}^{(t)}(i+1,j)}{3!} f'''\left(\lambda_0^{(t)}(i+1,j)\right)$$

$$+ \cdots + \frac{\left(\mu_1^{(t)}(i+1,j)\right)^{n-1}}{(n-1)!} f^{(n-1)}\left(\lambda_0^{(t)}(i+1,j)\right)$$

$$+ \mu_{n-1}^{(t)}(i-1,j) f'\left(\lambda_0^{(t)}(i-1,j)\right)$$

$$+ \frac{\sum_{i_1=1}^{n-2} \mu_{i_1}^{(t)}(i-1,j) \mu_{n-1-i_1}^{(t)}(i-1,j)}{2!} f''\left(\lambda_0^{(t)}(i-1,j)\right)$$

$$+ \frac{\sum_{1 \le i_1, i_2, i_3 \le n-3}^{i_1+i_2+i_3=n-1} \mu_{i_1}^{(t)}(i-1,j) \mu_{i_2}^{(t)}(i-1,j) \mu_{i_3}^{(t)}(i-1,j)}{3!} f'''\left(\lambda_0^{(t)}(i-1,j)\right)$$

$$+ \cdots + \frac{\left(\mu_1^{(t)}(i-1,j)\right)^{n-1}}{(n-1)!} f^{(n-1)}\left(\lambda_0^{(t)}(i-1,j)\right) \tag{12}$$

$$+ \mu_{n-1}^{(t)}(i,j+1) f'\left(\lambda_0^{(t)}(i,j+1)\right)$$

$$+ \frac{\sum_{i_1=1}^{n-2} \mu_{i_1}^{(t)}(i,j+1) \mu_{n-1-i_1}^{(t)}(i,j+1)}{2!} f''\left(\lambda_0^{(t)}(i,j+1)\right)$$

$$+ \frac{\sum_{1 \le i_1, i_2, i_3 \le n-3}^{i_1+i_2+i_3=n-1} \mu_{i_1}^{(t)}(i,j+1) \mu_{i_2}^{(t)}(i,j+1) \mu_{i_3}^{(t)}(i,j+1)}{3!} f'''\left(\lambda_0^{(t)}(i,j+1)\right)$$

$$+ \cdots + \frac{\left(\mu_1^{(t)}(i,j+1)\right)^{n-1}}{(n-1)!} f^{(n-1)}\left(\lambda_0^{(t)}(i,j+1)\right)$$

$$+ \mu_{n-1}^{(t)}(i,j-1) f'\left(\lambda_0^{(t)}(i,j-1)\right)$$

$$+ \frac{\sum_{i_1=1}^{n-2} \mu_{i_1}^{(t)}(i,j-1) \mu_{n-1-i_1}^{(t)}(i,j-1)}{2!} f''\left(\lambda_0^{(t)}(i,j-1)\right)$$

$$+ \frac{\sum_{1 \le i_1, i_2, i_3 \le n-3}^{i_1+i_2+i_3=n-1} \mu_{i_1}^{(t)}(i,j-1) \mu_{i_2}^{(t)}(i,j-1) \mu_{i_3}^{(t)}(i,j-1)}{3!} f'''\left(\lambda_0^{(t)}(i,j-1)\right)$$

$$+ \cdots + \frac{\left(\mu_1^{(t)}(i,j-1)\right)^{n-1}}{(n-1)!} f^{(n-1)}\left(\lambda_0^{(t)}(i,j-1)\right) \Bigg),$$

where indices (i,j) denote the coordinates of the current node $(i = 1, 2, \ldots, N_x, \ j = 1, 2, \ldots, N_y)$; $\lambda_0^{(0)}(i,j)$ is the recurrent eigenvalue of the matrix of initial conditions at the node (i,j); $\mu_1^{(0)}(i,j) \ne 0$.

3.1. The Hyper CML of the Logistic Maps.

Let us consider the scalar logistic map $x^{(t+1)} = ax^{(t)}(1 - x^{(t)})$ [63] with $0 < a \le 4$ and $0 \le x^{(0)} \le 1$. The scalar nodal variable of the logistic map is replaced by an $n \times n$ matrix with the largest divergence code $[0 \, 1 \, 2 \ldots (n-2)(n-1)]$. The iterative equations

defining the evolution of the logistic map are now reduced as higher derivatives of the scalar logistic mapping function do vanish:

$$\begin{cases} \lambda_0^{(t+1)} = a\lambda_0^{(t)}\left(1 - \lambda_0^{(t)}\right); \\ \mu_1^{(t+1)} = a\mu_1^{(t)}\left(1 - 2\lambda_0^{(t)}\right); \\ \mu_2^{(t+1)} = a\mu_2^{(t)}\left(1 - 2\lambda_0^{(t)}\right) - a\left(\mu_1^{(t)}\right)^2; \\ \cdots \\ \mu_{n-1}^{(t+1)} = a\mu_{n-1}^{(t)}\left(1 - 2\lambda_0^{(t)}\right) - a\sum_{i_1=1}^{n-2} \mu_{i_1}^{(t)} \mu_{n-1-i_1}^{(t)}; \end{cases} \tag{13}$$

TABLE 1: The CML generated at iteration t + 1 remains a hyper CML if the CML at iteration t is a hyper CML. The order of nodal matrices is $n = 2$; the coupling parameter $\varepsilon = 0.1$; the mapping function f is $x^{(t+1)} = 3.6x^{(t)}(1 - x^{(t)})$. The evolution of the CML is governed by equation (12).

Iteration t

Node	$\mathbf{X}^{(t)} = \lambda_0^{(t)}\mathbf{I} + \mu_1^{(t)}\mathbf{N}$	Eigenvalue $\lambda_0^{(t)}$	Parameter $\mu_1^{(t)}$	Nilpotent $\mathbf{N}$
(i, j)	$\mathbf{X}^{(t)} = \begin{bmatrix} 0.17 & 0.09 \\ -0.01 & 0.23 \end{bmatrix}$	$\lambda_0^{(t)} = 0.2$	$\mu_1^{(t)} = 0.1$	$\mathbf{N} = \begin{bmatrix} -0.3 & 0.9 \\ -0.1 & 0.3 \end{bmatrix}$
$(i+1, j)$	$\mathbf{X}^{(t)} = \begin{bmatrix} 0.18 & 0.36 \\ -0.04 & 0.42 \end{bmatrix}$	$\lambda_0^{(t)} = 0.3$	$\mu_1^{(t)} = 0.4$	$\mathbf{N} = \begin{bmatrix} -0.3 & 0.9 \\ -0.1 & 0.3 \end{bmatrix}$
$(i-1, j)$	$\mathbf{X}^{(t)} = \begin{bmatrix} 0.48 & 0.36 \\ -0.04 & 0.72 \end{bmatrix}$	$\lambda_0^{(t)} = 0.6$	$\mu_1^{(t)} = 0.4$	$\mathbf{N} = \begin{bmatrix} -0.3 & 0.9 \\ -0.1 & 0.3 \end{bmatrix}$
$(i, j+1)$	$\mathbf{X}^{(t)} = \begin{bmatrix} 0.55 & 0.45 \\ -0.05 & 0.85 \end{bmatrix}$	$\lambda_0^{(t)} = 0.7$	$\mu_1^{(t)} = 0.5$	$\mathbf{N} = \begin{bmatrix} -0.3 & 0.9 \\ -0.1 & 0.3 \end{bmatrix}$
$(i, j-1)$	$\mathbf{X}^{(t)} = \begin{bmatrix} 0.23 & 0.81 \\ -0.09 & 0.77 \end{bmatrix}$	$\lambda_0^{(t)} = 0.5$	$\mu_1^{(t)} = 0.9$	$\mathbf{N} = \begin{bmatrix} -0.3 & 0.9 \\ -0.1 & 0.3 \end{bmatrix}$

Iteration $t + 1$

Node	$\mathbf{X}^{(t+1)} = \lambda_0^{(t+1)}\mathbf{I} + \mu_1^{(t+1)}\mathbf{N}$	Eigenvalue $\lambda_0^{(t+1)}$	Parameter $\mu_1^{(t+1)}$	Nilpotent $\mathbf{N}$
(i, j)	$\mathbf{X}^{(t+1)} = \begin{bmatrix} 0.521 & 0.165 \\ -0.018 & 0.631 \end{bmatrix}$	$\lambda_0^{(t+1)} = 0.576$	$\mu_1^{(t+1)} = 0.1836$	$\mathbf{N} = \begin{bmatrix} -0.3 & 0.9 \\ -0.1 & 0.3 \end{bmatrix}$
$(i+1, j)$	$\mathbf{X}^{(t+1)} = \begin{bmatrix} 0.586 & 0.51 \\ -0.057 & 0.926 \end{bmatrix}$	$\lambda_0^{(t+1)} = 0.756$	$\mu_1^{(t+1)} = 0.567$	$\mathbf{N} = \begin{bmatrix} -0.3 & 0.9 \\ -0.1 & 0.3 \end{bmatrix}$
$(i-1, j)$	$\mathbf{X}^{(t+1)} = \begin{bmatrix} 0.918 & -0.162 \\ 0.018 & 0.81 \end{bmatrix}$	$\lambda_0^{(t+1)} = 0.864$	$\mu_1^{(t+1)} = -0.18$	$\mathbf{N} = \begin{bmatrix} -0.3 & 0.9 \\ -0.1 & 0.3 \end{bmatrix}$
$(i, j+1)$	$\mathbf{X}^{(t+1)} = \begin{bmatrix} 0.93 & -0.52 \\ 0.058 & 0.582 \end{bmatrix}$	$\lambda_0^{(t+1)} = 0.756$	$\mu_1^{(t+1)} = -0.578$	$\mathbf{N} = \begin{bmatrix} -0.3 & 0.9 \\ -0.1 & 0.3 \end{bmatrix}$
$(i, j-1)$	$\mathbf{X}^{(t+1)} = \begin{bmatrix} 0.884 & 0.05 \\ -0.005 & 0.916 \end{bmatrix}$	$\lambda_0^{(t+1)} = 0.9$	$\mu_1^{(t+1)} = 0.054$	$\mathbf{N} = \begin{bmatrix} -0.3 & 0.9 \\ -0.1 & 0.3 \end{bmatrix}$

where $\mu_1^{(0)} \neq 0$.

Let us construct a hyper CML of logistic maps on the rectangular domain $[1, N_x] \times [1, N_y]$. The governing equations of a hyper CML follow from (13):

$$\lambda_0^{(t+1)}(i, j) = a\lambda_0^{(t)}(i, j)\left(1 - \lambda_0^{(t)}(i, j)\right),$$

$$\mu_1^{(t+1)}(i, j) = (1 - \varepsilon)a\mu_1^{(t)}(i, j)\left(1 - 2\lambda_0^{(t)}(i, j)\right)$$

$$+ \frac{\varepsilon}{4}\left(a\mu_1^{(t)}(i + 1, j)\left(1 - 2\lambda_0^{(t)}(i + 1, j)\right)\right.$$

$$+ a\mu_1^{(t)}(i - 1, j)\left(1 - 2\lambda_0^{(t)}(i - 1, j)\right)$$

$$+ a\mu_1^{(t)}(i, j + 1)\left(1 - 2\lambda_0^{(t)}(i, j + 1)\right)$$

$$+ a\mu_1^{(t)}(i, j - 1)\left(1 - 2\lambda_0^{(t)}(i, j - 1)\right)\bigg),$$

$$\mu_2^{(t+1)}(i, j) = (1 - \varepsilon)\left(a\mu_2^{(t)}(i, j)\left(1 - 2\lambda_0^{(t)}(i, j)\right) - a\left(\mu_1^{(t)}(i, j)\right)^2\right)$$

$$+ \frac{\varepsilon}{4}\left(a\mu_2^{(t)}(i + 1, j)\left(1 - 2\lambda_0^{(t)}(i + 1, j)\right) - a\left(\mu_1^{(t)}(i + 1, j)\right)^2\right.$$

$$+ a\mu_2^{(t)}(i - 1, j)\left(1 - 2\lambda_0^{(t)}(i - 1, j)\right) - a\left(\mu_1^{(t)}(i - 1, j)\right)^2$$

$$+ a\mu_2^{(t)}(i, j + 1)\left(1 - 2\lambda_0^{(t)}(i, j + 1)\right) - a\left(\mu_1^{(t)}(i, j + 1)\right)^2$$

$$+ a\mu_2^{(t)}(i, j - 1)\left(1 - 2\lambda_0^{(t)}(i, j - 1)\right) - a\left(\mu_1^{(t)}(i, j - 1)\right)^2\bigg),$$

$$\cdots$$

$$\mu_{n-1}^{(t+1)}(i, j) = (1 - \varepsilon)\left(a\mu_{n-1}^{(t)}(i, j)\left(1 - 2\lambda_0^{(t)}(i, j)\right)\right. \tag{14}$$

$$-a\sum_{i_1=1}^{n-2}\mu_{i_1}^{(t)}(i, j)\mu_{n-1-i_1}^{(t)}(i, j)\Bigg)$$

$$\frac{\varepsilon}{4}\left(a\mu_{n-1}^{(t)}(i + 1, j)\left(1 - 2\lambda_0^{(t)}(i + 1, j)\right)\right.$$

$$- a\sum_{i_1=1}^{n-2}\mu_{i_1}^{(t)}(i + 1, j)\mu_{n-1-i_1}^{(t)}(i + 1, j)$$

$$+ a\mu_{n-1}^{(t)}(i - 1, j)\left(1 - 2\lambda_0^{(t)}(i - 1, j)\right)$$

$$- a\sum_{i_1=1}^{n-2}\mu_{i_1}^{(t)}(i - 1, j)\mu_{n-1-i_1}^{(t)}(i - 1, j)$$

$$+ a\mu_{n-1}^{(t)}(i, j + 1)\left(1 - 2\lambda_0^{(t)}(i, j + 1)\right)$$

$$- a\sum_{i_1=1}^{n-2}\mu_{i_1}^{(t)}(i, j + 1)\mu_{n-1-i_1}^{(t)}(i, j + 1)$$

$$+ a\mu_{n-1}^{(t)}(i, j - 1)\left(1 - 2\lambda_0^{(t)}(i, j - 1)\right)$$

$$- a\sum_{i_1=1}^{n-2}\mu_{i_1}^{(t)}(i, j - 1)\mu_{n-1-i_1}^{(t)}(i, j - 1)\Bigg),$$

where indices (i, j) denote the coordinates of the current node $(i = 1, 2, \ldots, N_x, \ j = 1, 2, \ldots, N_y)$; $\lambda_0^{(0)}(i, j)$ is the recurrent eigenvalue of the matrix of initial conditions at the node (i, j); $\mu_1^{(0)}(i, j) \neq 0$.

4. The Construction of the Multiple Image Hiding Scheme Based on Hyper CML

Without loss of generality let us consider the logistic map of nilpotent matrices of order 4 with the largest divergence code $\begin{bmatrix} 0 & 1 & 2 & 3 \end{bmatrix}$ (all four eigenvalues of the matrix of initial conditions do coincide) [56]. Let us denote the repetitive eigenvalue of the matrix of initial conditions as $\lambda_0^{(0)}$:

$$\mathbf{X}^{(0)} = \lambda_0^{(0)}\mathbf{I} + \mu_1^{(0)}\mathbf{N}_1 + \mu_2^{(0)}\mathbf{N}_2 + \mu_3^{(0)}\mathbf{N}_3, \quad (15)$$

where $\mathbf{N}_1 = \mathbf{T}\begin{bmatrix} 0 & 1 & 0 & 0 \\ 0 & 0 & 1 & 0 \\ 0 & 0 & 0 & 1 \\ 0 & 0 & 0 & 0 \end{bmatrix}\mathbf{T}^{-1}$, $\mathbf{N}_2 = \mathbf{T}\begin{bmatrix} 0 & 0 & 1 & 0 \\ 0 & 0 & 0 & 1 \\ 0 & 0 & 0 & 0 \\ 0 & 0 & 0 & 0 \end{bmatrix}\mathbf{T}^{-1}$, and

$\mathbf{N}_3 = \mathbf{T}\begin{bmatrix} 0 & 0 & 0 & 1 \\ 0 & 0 & 0 & 0 \\ 0 & 0 & 0 & 0 \\ 0 & 0 & 0 & 0 \end{bmatrix}\mathbf{T}^{-1}$; $\mathbf{T}$ is a nonsingular square matrix of

order 4; $\mu_1^{(0)}$, $\mu_2^{(0)}$, and $\mu_3^{(0)}$ are the auxiliary parameters not equal to zero.

4.1. The Logistic Map of Nilpotent Matrices of Order 4.
The dynamics of the iterative logistic map of matrices of order 4 splits into four scalar intertwined iterative maps (13):

$$\begin{cases} \lambda_0^{(t+1)} = a\lambda_0^{(t)}\left(1 - \lambda_0^{(t)}\right), \\ \mu_1^{(t+1)} = a\mu_1^{(t)}\left(1 - 2\lambda_0^{(t)}\right), \\ \mu_2^{(t+1)} = a\mu_2^{(t)}\left(1 - 2\lambda_0^{(t)}\right) - a\left(\mu_1^{(t)}\right)^2, \\ \mu_3^{(t+1)} = a\mu_3^{(t)}\left(1 - 2\lambda_0^{(t)}\right) - 2a\mu_1^{(t)}\mu_2^{(t)}. \end{cases} \quad (16)$$

The necessary and sufficient conditions for the iterative map of matrices of order n to diverge are [56]:

(i) The packing code must be greater than zero (at least two eigenvalues of the matrix of initial conditions must coincide)

(ii) The Lyapunov exponent of the scalar iterative map must be greater than zero (the iterative map must generate a chaotic process)

The first condition for (16) is satisfied automatically. The Lyapunov exponent for the scalar logistic map reads [64]:

$$L = \frac{1}{t} \sum_{s=0}^{t-1} \ln\left(a\left|1 - 2\lambda_0^{(s)}\right|\right). \quad (17)$$

Let us observe that

$$\ln\left(\left|\mu_1^{(t+1)}\right|\right) = \ln\left(\prod_{s=0}^{t}\left|f'\left(\lambda_0^{(s)}\right)\right|\right) = L(t + 1). \quad (18)$$

If the Lyapunov exponent L is greater than zero, then the sequence $|\mu_1^{(t)}|$ will diverge. The divergence rate of $|\mu_1^{(t)}|$ is linear the growth of the elements of the sequence $|\mu_1^{(t)}|$ is comparable (in average) to the growth rate of a geometric progression (the common ratio of this progression is L). Then, the slope of the approximating line describing the growth of $\ln|\mu_1^{(t)}|$ is L.

The growth rate of $|\mu_2^{(t)}|$ can be evaluated analogously. The term $|a\mu_2^{(t)}(1 - 2\lambda_0^{(t)})|$ vanishes in respect of $|a(\mu_1^{(t)})^2|$ at large t (note that $\mu_2^{(0)} \neq 0$). Then,

$$\lim_{t \to \infty} \ln\left|\mu_2^{(t)}\right| = \ln(a) + 2\lim_{t \to \infty} \ln\left|\mu_1^{(t)}\right|. \quad (19)$$

Therefore, the slope of a line approximating the average growth of $\ln|\mu_2^{(t)}|$ is $2L$ (at large t). Analogously,

$$\lim_{t \to \infty} \ln\left|\mu_3^{(t)}\right| = \ln(2a) + \lim_{t \to \infty} \ln\left|\mu_1^{(t)}\right| + \lim_{t \to \infty} \ln\left|\mu_2^{(t)}\right|. \quad (20)$$

Thus, the slope of a line approximating the average growth of $\ln|\mu_3^{(t)}|$ is $3L$. The divergence of the logistic map of matrices of order 4 is illustrated in Figure 1. The divergence rate of auxiliary parameters $\mu_1^{(t)}$, $\mu_2^{(t)}$, and $\mu_3^{(t)}$ at $a = 3.59$ are presented in Figure 2. It can be observed that formal evaluation of the divergence rates of auxiliary parameters $\mu_1^{(t)}$, $\mu_2^{(t)}$, and $\mu_3^{(t)}$ does correspond well to the results of computational simulations.

4.2. The Proposed Image Hiding Scheme in a Hyper CML.
Let us consider the coupling between auxiliary parameters $\mu_1^{(t)}$, $\mu_2^{(t)}$, and $\mu_3^{(t)}$ as defined by equation (16). These relationships are represented by the schematic diagram in Figure 3. The evolution of $\mu_1^{(t+1)}$ depends on $\mu_1^{(t)}$ but is affected neither by $\mu_2^{(t)}$ nor by $\mu_3^{(t)}$.

Analogously, the evolution of $\mu_2^{(t+1)}$ depends on $\mu_1^{(t)}$ and $\mu_2^{(t)}$–but is not affected by $\mu_3^{(t)}$. Finally, the evolution of $\mu_3^{(t+1)}$ is affected by $\mu_1^{(t)}$ and $\mu_2^{(t)}$, and by $\mu_3^{(t)}$.

Such complex interconnections between auxiliary parameters enable the construction of the hiding scheme of multiple images in one single hyper CML.

Initially, let us observe the effects caused by perturbations in $\mu_1^{(0)}$ to the evolution of $\mu_1^{(t)}$, $\mu_2^{(t)}$, and $\mu_3^{(t)}$ (Figure 4). At first, initial conditions of $\mu_1^{(0)}(i, j)$, $\mu_2^{(0)}(i, j)$, and $\mu_3^{(0)}(i, j)$ are set to 0 in the whole domain. Then, the dot skeleton representation of the secret image is embedded into the hyper CML by perturbing initial conditions of $\mu_1^{(0)}(i, j)$ at the nodes corresponding to the dot skeleton representation of the secret image. The parameters ε and a of the hyper CML are set to 0.13 and 3.59 accordingly at all the nodes of the domain. Patterns produced after 10, 20, 50, 100, 200, 300, 400, and 600 time-forward iterations are depicted in Figure 4.

The secret image is underdeveloped in the parameter plane of $\mu_1^{(t)}(i, j)$ at $t = 10, 20, 50$ (Figure 4). However, the pattern representing the secret image gets overdeveloped at $t > 200$ (Figure 4).
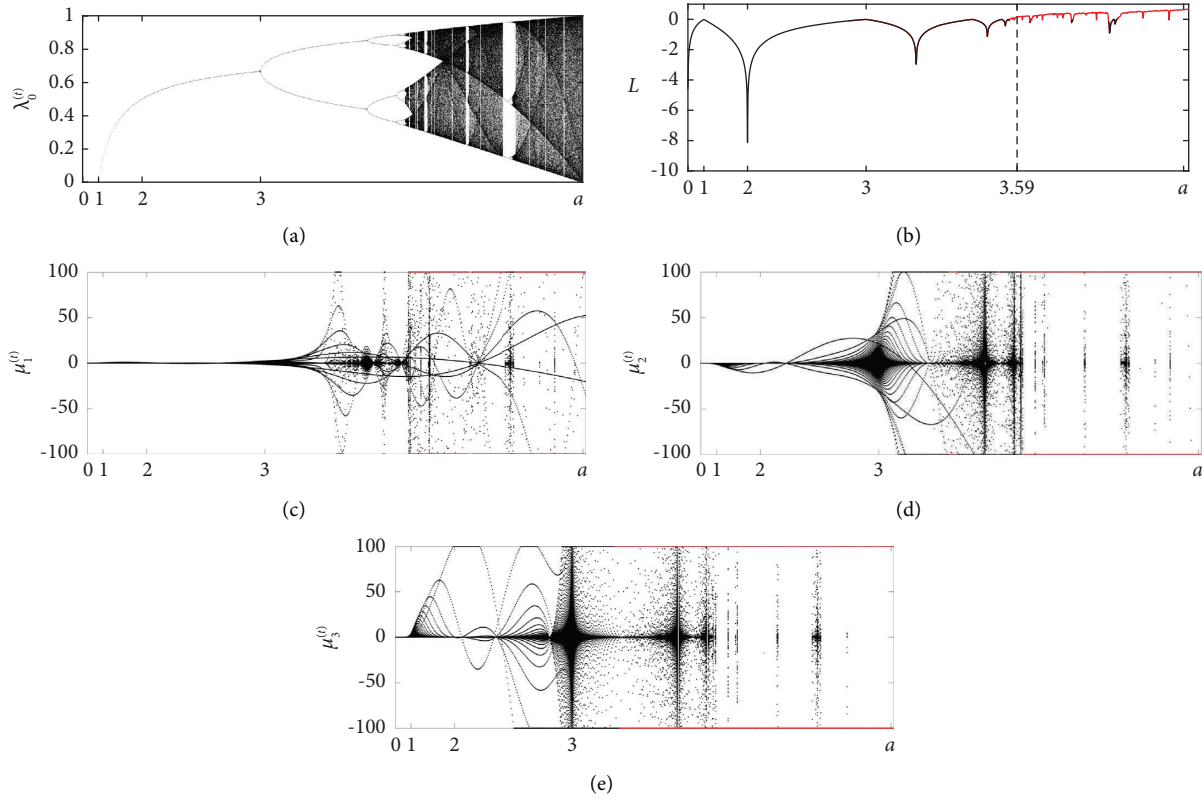
(a)

(b)

(c)

(d)

(e)
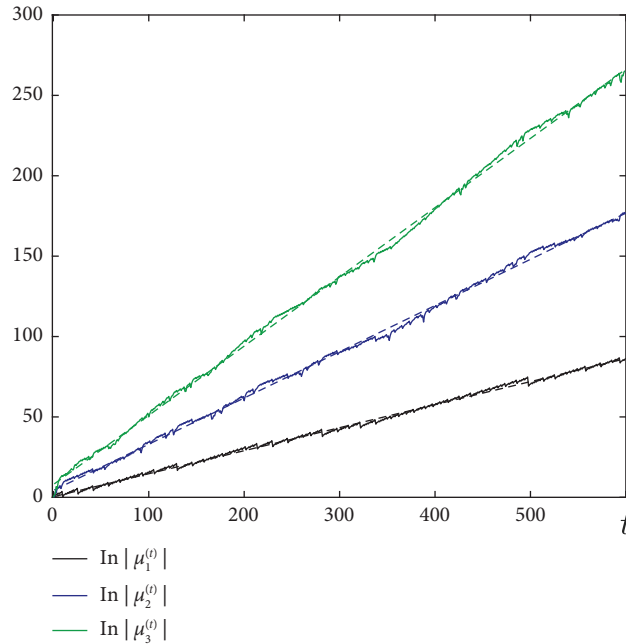
FIGURE 1: The divergence of the logistic map of nilpotent matrices of order 4. The recurrent eigenvalue of the matrix of initial conditions $\lambda_0^{(0)}$ is set to 0.1. The bifurcation diagram of the scalar logistic map $\lambda_0^{(t+1)} = a\lambda_0^{(t)}(1 - \lambda_0^{(t)})$ is depicted in part (a); the Lyapunov exponent for this map is represented in part (b) (values greater than zero are marked in red). Initial values of auxiliary parameters $\mu_1^{(0)}$, $\mu_2^{(0)}$, and $\mu_3^{(0)}$ are set to 1. The evolution of auxiliary parameters $\mu_1^{(t)}$, $\mu_2^{(t)}$, and $\mu_3^{(t)}$ is shown in parts (c–e) accordingly. Absolute values of auxiliary parameters $\mu_1^{(t)}$, $\mu_2^{(t)}$, and $\mu_3^{(t)}$ greater than 100 are cut off at 100 for the clarity of visualization. Absolute values of auxiliary parameters $\mu_1^{(t)}$, $\mu_2^{(t)}$, and $\mu_3^{(t)}$ greater than 10^5 are marked in red.

FIGURE 2: The rate of divergence the logistic map of nilpotent matrices of order 4. The recurrent eigenvalue of the matrix of initial conditions $\lambda_0^{(0)}$ is set to 0.1; a is set to 3.59; initial values of auxiliary parameters $\mu_1^{(0)}$, $\mu_2^{(0)}$, and $\mu_3^{(0)}$ are set to 1. The Lyapunov exponent L of the scalar logistic map is 0.139 at $a = 3.59$. The evolution of $\ln|\mu_1^{(t)}|$, $\ln|\mu_2^{(t)}|$, and $\ln|\mu_3^{(t)}|$ is represented by the black line, the blue line, and the green line, respectively. The growth of $\ln|\mu_1^{(t)}|$ is approximated by the black dashed line with the slope coefficient equal to $0.143 \approx L$. The growth of $\ln|\mu_2^{(t)}|$ is approximated by the blue dashed line with the slope coefficient equal to $0.285 \approx 2L$. The growth of $\ln|\mu_3^{(t)}|$ is approximated by the green dashed line with the slope coefficient equal to $0.431 \approx 3L$.
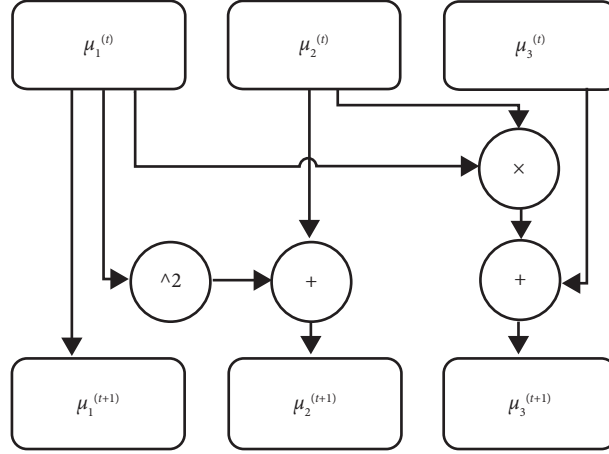
FIGURE 3: The schematic diagram of relationships between auxiliary parameters $\mu_1^{(t)}$, $\mu_2^{(t)}$, and $\mu_3^{(t)}$ according to (16).
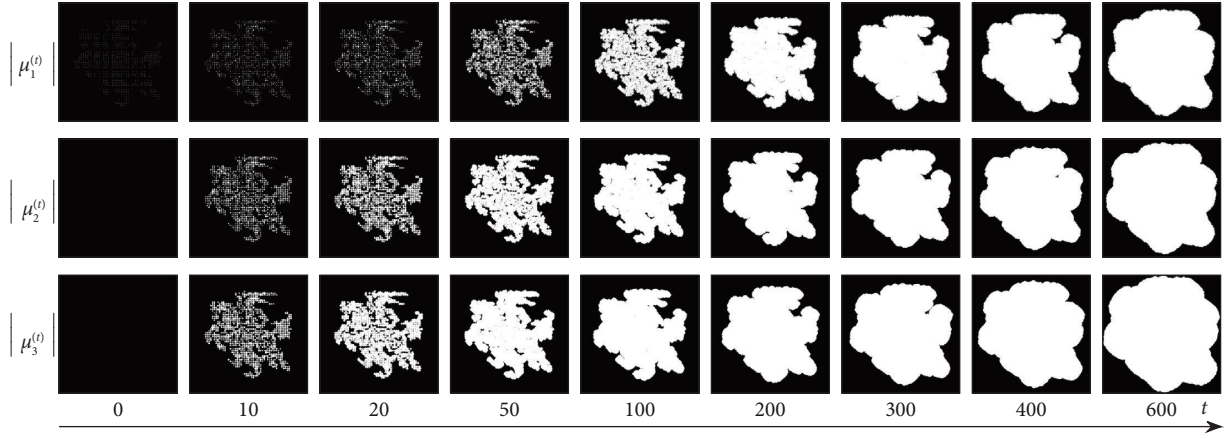

FIGURE 4: Perturbations in the parameter plane $\mu_1^{(0)}(i, j)$ are transmitted into parameter planes $\mu_2^{(t)}(i, j)$ and $\mu_3^{(t)}(i, j)$ ($\varepsilon = 0.13$; $a = 3.59$). Initial conditions of $\mu_1^{(0)}$, $\mu_2^{(0)}$, and $\mu_3^{(0)}$ are set to zero in the whole domain. The dot skeleton representation of the secret image is embedded into the hyper CML by setting initial conditions $\mu_1^{(0)}(i, j) = 1$ at the nodes corresponding to the dot skeleton representation of the secret image. The produced patterns are depicted after 10, 20, 50, 100, 200, 300, 400, and 600 time-forward iterations.

It can be observed that the perturbations in the parameter plane of $\mu_1^{(0)}(i, j)$ are transmitted into the parameter plane of $\mu_2^{(t)}(i, j)$ and the parameter plane of $\mu_3^{(t)}(i, j)$ (Figure 4). The random mean square error (RMSE) between the inverse original secret image and the patterns produced in parameter planes $\mu_1^{(t)}(i, j)$, $\mu_2^{(t)}(i, j)$, and $\mu_3^{(t)}(i, j)$ help to determine the optimal time steps when the developed patterns yield the best correspondence to the secret image (Figure 5). Note that the optimal time moments are different for all three parameter planes (Figure 5).

Further, let us investigate the effects caused by perturbations in $\mu_2^{(0)}$ to the evolution of $\mu_1^{(t)}$, $\mu_2^{(t)}$, and $\mu_3^{(t)}$ (Figure 6). The initial conditions of $\mu_2^{(0)}(i, j)$, and $\mu_3^{(0)}(i, j)$ are set to 0 in the whole domain. The dot skeleton representation of the secret image is embedded into the hyper CML by perturbing initial conditions of $\mu_2^{(0)}(i, j)$ at the nodes corresponding to the dot skeleton representation of the secret image. Note that initial values of $\mu_1^{(0)}(i, j)$ are set to 0.0001 in the whole domain. The parameters ε and a of the hyper CML are set to the same values as before. Patterns produced after

10, 20, 50, 100, 200, 300, 400, and 600 time-forward iterations are depicted in Figure 6.

The secret image is underdeveloped in the parameter plane $\mu_2^{(t)}(i, j)$ at $t < 10$ (Figure 6). However, the pattern representing the secret image gets noninterpretable at $t \geq 200$ due to the divergence of $\mu_2^{(t)}(i, j)$ (Figure 6). Perturbations in the parameter plane $\mu_2^{(0)}(i, j)$ are transmitted into the parameter plane $\mu_3^{(t)}(i, j)$ (Figure 6). Note that the secret image is not transmitted back into the parameter plane $\mu_1^{(t)}(i, j)$. The RMSE values between the inverse of the secret image and the patterns produced in parameter planes $\mu_2^{(t)}(i, j)$ and $\mu_3^{(t)}(i, j)$ help to identify the optimal time steps when the developed patterns yield the closest reconstruction of the secret image (Figure 7).

Finally, let us present the multiple images hiding scheme in the proposed hyper CML. At first, initial conditions of $\mu_1^{(0)}(i, j)$, $\mu_2^{(0)}(i, j)$, and $\mu_3^{(0)}(i, j)$ are set to 0 in the whole domain. Then, dot skeleton representations of three different secret images (Coat of Arms, Radioactive, and At Sign) are embedded into the hyper CML. Initial conditions of
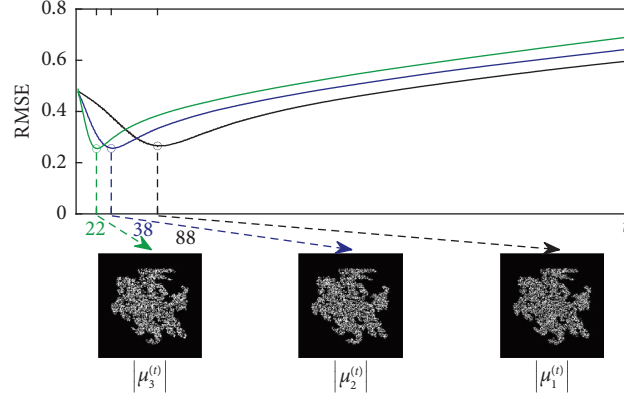
FIGURE 5: The RMSE between the original secret image and patterns produced in parameter planes $|\mu_1^{(t)}|$, $|\mu_2^{(t)}|$, and $|\mu_3^{(t)}|$ help to determine the optimal time steps ($t = 88$, $t = 38$, and $t = 22$) when the developed patterns yield the best correspondence to the secret image.
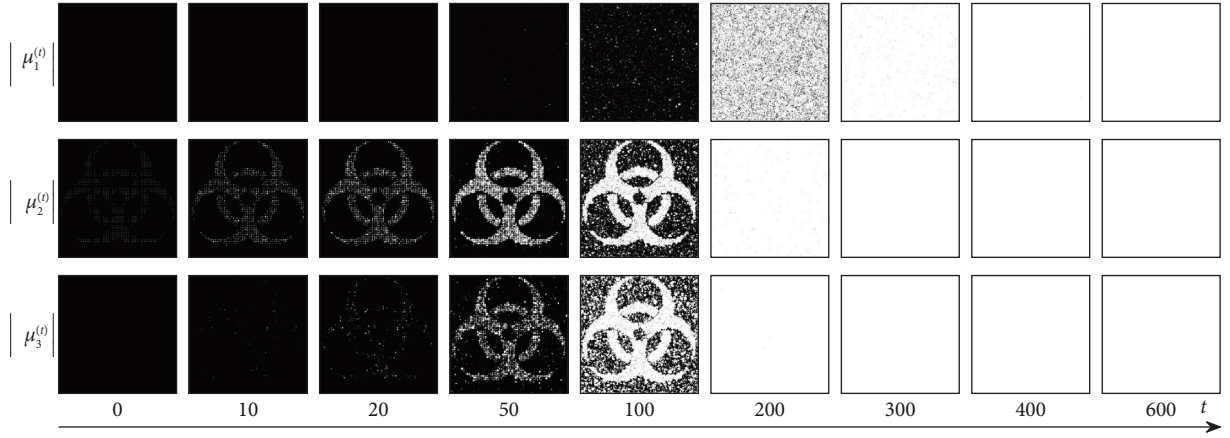

FIGURE 6: Perturbations in the parameter plane $\mu_2^{(0)}(i, j)$ are transmitted into the parameter plane $\mu_3^{(t)}(i, j)$ but not in to the parameter plane $\mu_1^{(t)}(i, j)$ ($\varepsilon = 0.13$; $a(i, j) = 3.59$). Initial conditions of $\mu_1^{(0)}$ are set to 0.0001; initial conditions of $\mu_2^{(0)}$ and $\mu_3^{(0)}$ are set to zero in the whole domain. The dot skeleton representation of the secret image is embedded into the hyper CML by setting initial conditions $\mu_2^{(0)}(i, j) = 1$ at the nodes corresponding to the dot skeleton representation of the secret image. The produced patterns are depicted after 10, 20, 50, 100, 200, 300, 400, and 600 time-forward iterations.
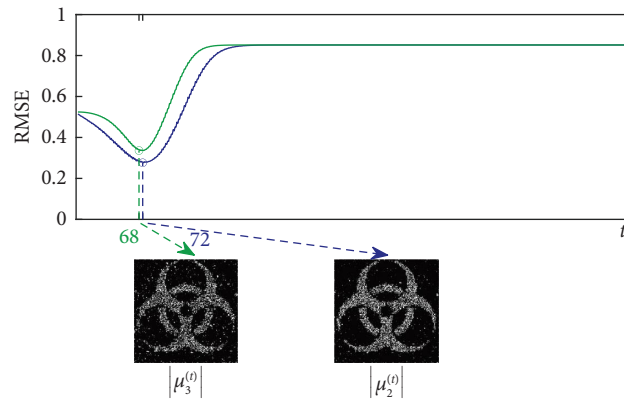
FIGURE 7: The RMSE values between the original image and patterns produced in parameter planes $|\mu_2^{(t)}|$ and $|\mu_3^{(t)}|$ help to determine the optimal time steps ($t = 72$ and $t = 68$) when the developed patterns yield the best correspondence to the secret image.

$\mu_1^{(0)}(i, j)$ are perturbed by the dot skeleton representation of the Coat of Arms, initial conditions of $\mu_2^{(0)}(i, j)$ are perturbed by the dot skeleton representation of the Radioactive, and initial conditions of $\mu_3^{(0)}(i, j)$ are perturbed by the dot skeleton representation of the At Sign at nodes corresponding to dot skeleton representations of the secret

images. The parameters ε and a of the hyper CML are set to 0.13 and 3.59 accordingly at all the nodes of the domain. Patterns produced after 10, 20, 50, 100, 200, 300, 400, and 600 time-forward iterations are depicted in Figure 8.

The best representation of the Coat of Arms is achieved at $t = 271$ in the parameter plane $\mu_1^{(t)}$ (Figure 9). The best representation of the secret image Radioactive is achieved at $t = 91$ in the parameter plane $\mu_2^{(t)}$ (Figure 9). However, the Radioactive pattern is soon contaminated afterwards by the Coat of Arms (transmitted from the parameter plane $\mu_1^{(t)}$) (Figure 9). The best representation of the At Sign is achieved at $t = 60$ in the parameter plane $\mu_3^{(t)}$ (Figure 9). The pattern in $\mu_3^{(t)}$ is quickly contaminated afterwards by the information transmitted from the parameter planes $\mu_1^{(t)}$ and $\mu_2^{(t)}$ (Figure 9).

4.3. The Structured Diagram of the Communication Scheme Based on a Hyper CML

4.3.1. The Communication Scheme. The structure of communication scheme between Bob (the sender) and Alice (the receiver) reads:

Step 1. Hiding multiple images into the initial conditions of the hyper CLM.

Bob generates the initial conditions for the hyper CLM and hides all different secret images into the matrix of initial conditions.

(i) Define the resolution of the image (the spatial dimension or the number of the nodes in the hyper CML): $N_x \times N_y$.

(ii) Define the nodal dimension of the hyper CML (the size of the nodal matrix $n \times n$; $n \geq 2$). Without loss of generality all further instructions are limited to $n = 4$ (the carrying capacity of the scheme is $n - 1 = 3$ secret images).

(iii) Set
$$\mathbf{I} = \begin{bmatrix} 1 & 0 & 0 & 0 \\ 0 & 1 & 0 & 0 \\ 0 & 0 & 1 & 0 \\ 0 & 0 & 0 & 1 \end{bmatrix}; \quad \mathbf{N}_1 = \begin{bmatrix} 0 & 1 & 0 & 0 \\ 0 & 0 & 1 & 0 \\ 0 & 0 & 0 & 1 \\ 0 & 0 & 0 & 0 \end{bmatrix};$$
$$\mathbf{N}_2 = \begin{bmatrix} 0 & 0 & 1 & 0 \\ 0 & 0 & 0 & 1 \\ 0 & 0 & 0 & 0 \\ 0 & 0 & 0 & 0 \end{bmatrix}; \quad \mathbf{N}_3 = \begin{bmatrix} 0 & 0 & 0 & 1 \\ 0 & 0 & 0 & 0 \\ 0 & 0 & 0 & 0 \\ 0 & 0 & 0 & 0 \end{bmatrix}.$$

(iv) Define the scalar iterative chaotic map. The presented computational experiment in this paper uses the logistic map.

(v) Set the hyper CML to the onset of chaos. The parameter of the scalar logistic map **a** is set to 3.59 in the computational experiment presented in this paper.

(vi) Set the coupling parameter of the hyper CML to such a value which guarantees the effect of the finite-time divergence in the spatial surrounding of the perturbed nodes. The parameter ε is set to 0.13 in the computational experiment presented in this paper.

(vii) Generate three $N_x \times N_y$ dimensional sparse logical matrices (masks) $\mathbf{M}_1$, $\mathbf{M}_2$, and $\mathbf{M}_3$-the dot skeleton representations of secret image 1, secret image 2, and secret image 3. The elements of the masks are zeros except the points corresponding to the dot skeleton representations of the secret images.

(viii) Define the magnitude of perturbation $\mu_1^{(0)}$, $\mu_2^{(0)}$, and $\mu_3^{(0)}$ for mask 1, mask 2, and mask 3. The presented computational experiment in this paper assumes $\mu_1^{(0)} = 0.0001$; $\mu_2^{(0)} = 1$; $\mu_3^{(0)} = 10$.

(ix) Define the seed for random generator to produce the $N_x \times N_y$ dimensional matrix of eigenvalues $0 < \lambda_0 < 1$ and a random nonsingular four-dimensional square matrix $\mathbf{T}$.

(x) For each node (i, j) of the hyper CML, expand each scalar node to a 4×4 nodal matrix $\mathbf{H}_{i,j}$: $\mathbf{H}_{i,j} = \mathbf{T}(\lambda_0^{(0)}I + \mu_1^{(0)}\mathbf{M}_1(i, j)\mathbf{N}_1 + \mu_2^{(0)}\mathbf{M}_2(i, j)\mathbf{N}_2 + \mu_3^{(0)}\mathbf{M}_3(i, j)\mathbf{N}_3)\mathbf{T}^{-1}$.

(xi) The resulting $N_x \times N_y$ dimensional matrix $\mathbf{H}$ does represent the initial conditions of the hyper CML (the cover image C).

(xii) Set the number of time-forward iterations t_1, t_2, and t_3 required to reveal secret image 1, secret image 2, and secret image 3. The presented computational experiment in this paper assumes $t_1 = 271$, $t_2 = 91$, and $t_3 = 60$.

Step 2. Transmit the cover image C to the receiver. Transmit the parameters of the hyper CML to the receiver.

The cover image C can be considered as a public key. The eavesdroppers would need to know that the cover image does represent the initial conditions of the hyper CML. Also, the eavesdroppers would need to know the spatial dimension of the hyper CML $N_x \times N_y$, the nodal dimension of the hyper CML n, and all the parameters of the hyper CML to be able to decode the secret images.

The parameters of the hyper CML (the spatial dimension of the hyper CML, the nodal dimension of the hyper CML n, the parameter of the chaotic iterative map a, the coupling parameter ε, the number of time-forward iterations t_1, t_2, t_3) can be considered as private keys.

Step 3. Run the hyper CML and decode the secret images.

Alice can decode the secret images if and only if she is running the hyper CML with preset parameters on the matrix of initial conditions received from Bob. As soon as the given number of time-forward iterations t_k is reached, Alice needs to decompose each nodal matrix of the hyper CML to the combination of the diagonal matrix and the combination of nilpotent. The weighting coefficient (the auxiliary parameter) of the k-th nilpotent μ_k will define the
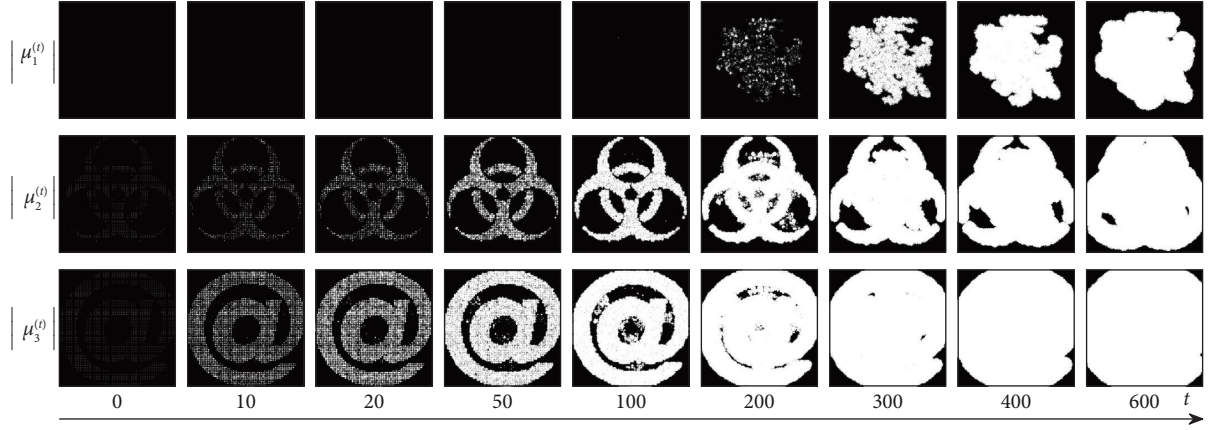
FIGURE 8: The hiding scheme of tree different secret images into a single hyper CML ($\varepsilon = 0.13$; $a = 3.59$). Initial conditions of $\mu_1^{(0)}$, $\mu_2^{(0)}$, and $\mu_3^{(0)}$ are set to zero in the whole domain. Initial conditions of $\mu_1^{(0)}$ are perturbed by setting $\mu_1^{(0)}(i, j) = 0.0001$ at nodes corresponding to the dot skeleton representation of the Coat of Arms. Initial conditions of $\mu_2^{(0)}$ are perturbed by setting $\mu_2^{(0)}(i, j) = 1$ at nodes corresponding to the dot skeleton representation of the Radioactive. Initial conditions of $\mu_3^{(0)}$ are perturbed by setting $\mu_3^{(0)}(i, j) = 10$ at nodes corresponding to the dot skeleton representation of the At Sign. The produced patterns are depicted after 10, 20, 50, 100, 200, 300, 400, and 600 time-forward iterations.
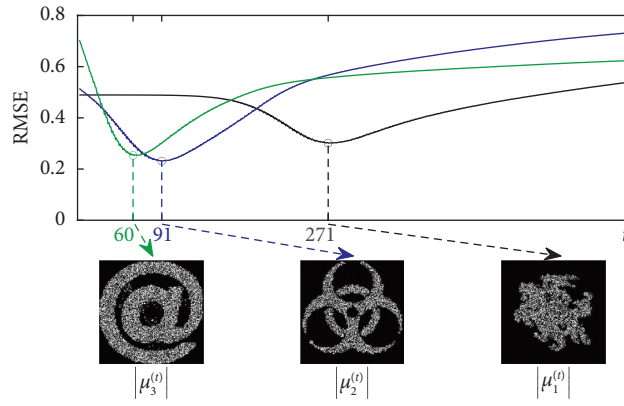
FIGURE 9: The hiding scheme of tree different secret images into a single hyper CML. The Coat of Arms is revealed at $t = 271$ in the parameter plane $|\mu_1^{(t)}|$. The Radioactive is revealed at $t = 91$ in the parameter plane $|\mu_2^{(t)}|$. The At Sign is revealed at $t = 60$ in the parameter plane $|\mu_3^{(t)}|$.
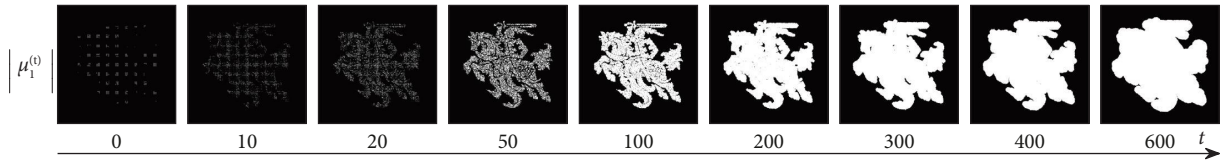

FIGURE 10: The dot skeleton representation of the Coat of Arms is embedded in the hyper CML with the nodal dimension of 2 ($\varepsilon = 0.13$; $a = 3.59$). The initial conditions of $\mu_1^{(0)}$ are set to zero in the whole domain; the perturbation magnitude at dot skeleton is set to 1. The produced patterns are depicted after 10, 20, 50, 100, 200, 300, 400, and 600 time-forward iterations (the best reconstruction of the secret image is reached after 92 iterations).

brightness of the pixel of the k-th secret image (the coordinates of the pixel do correspond to the indexes of the current node of the hyper CML).

4.3.2. The Dot Skeleton Representation of the Secret Images.
Each secret image must be transformed into its dot skeleton representation before it is embedded into the hyper CML.

The dot skeleton representation must satisfy the following two opposite requirements [65]:

(i) The points of the dot skeleton representation should be as far from each other as possible.

(ii) The points of the dot skeleton representation should not be located too far from each other so that the

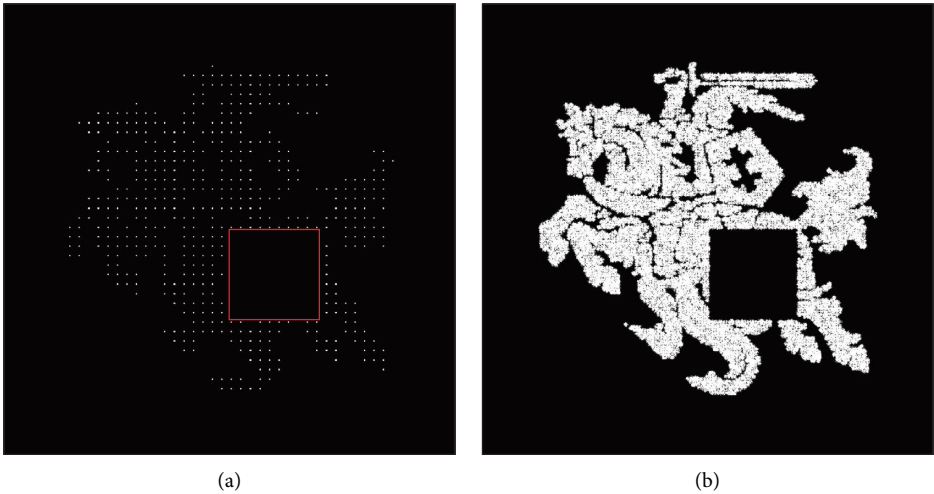(a)   (b)

FIGURE 11: The secret information is lost only within the cropped part of the secret image. Part (a) represents the dot skeleton of the secret image with a cropped square marked in red; part (b) shows the decoded secret image.
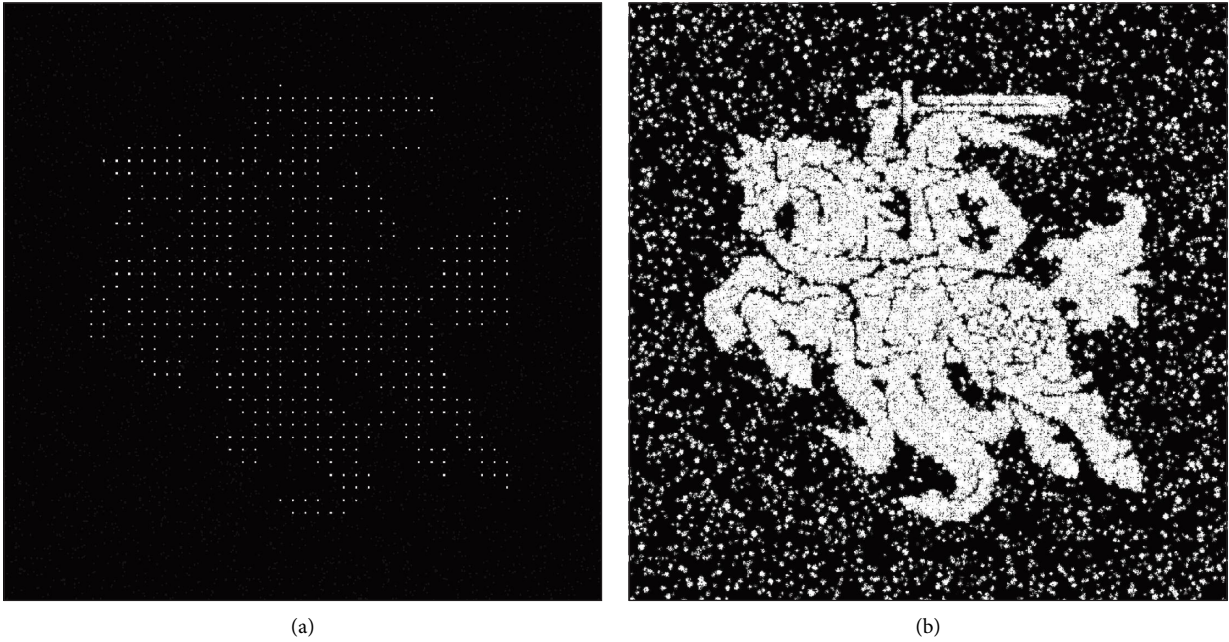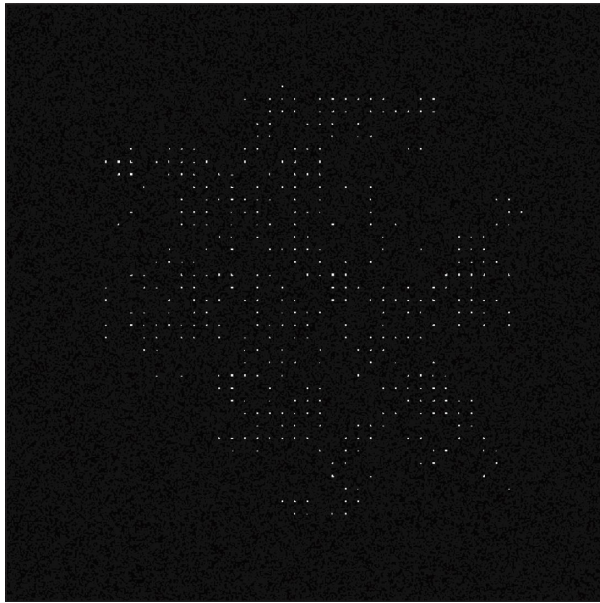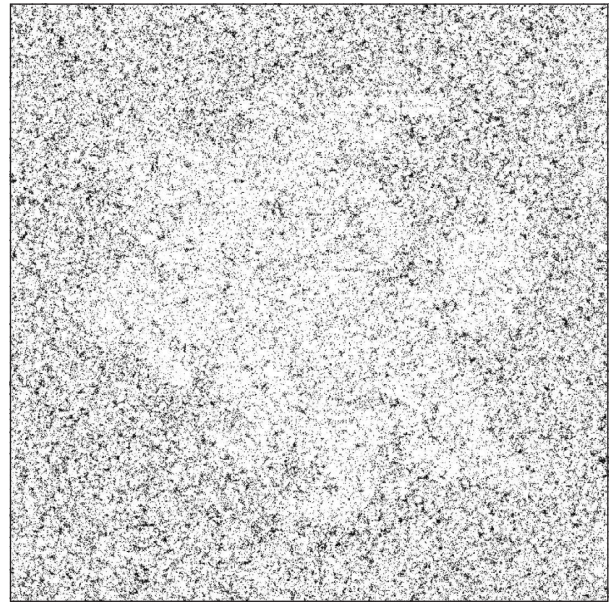

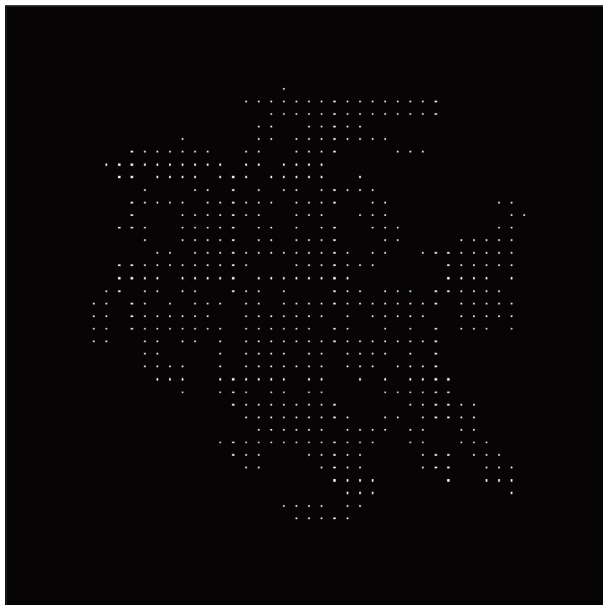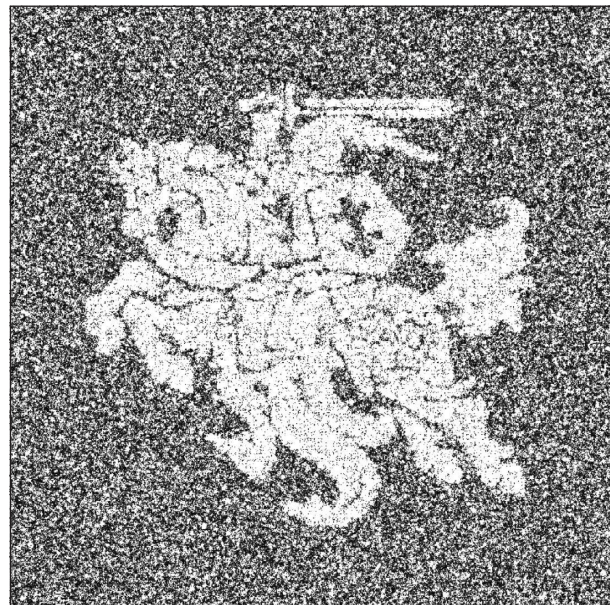(a)   (b)

FIGURE 12: Continued.

(c)

(d)

Figure 12: The "salt and pepper" type noise added to the dot skeleton image partially and fully destroys the decoded secret. Dot skeletons images with 1% and 25% of pixels affected with the noise are depicted in parts (a) and (c) accordingly. The decoded images are shown in panels (b) and (d).

(a)

(b)
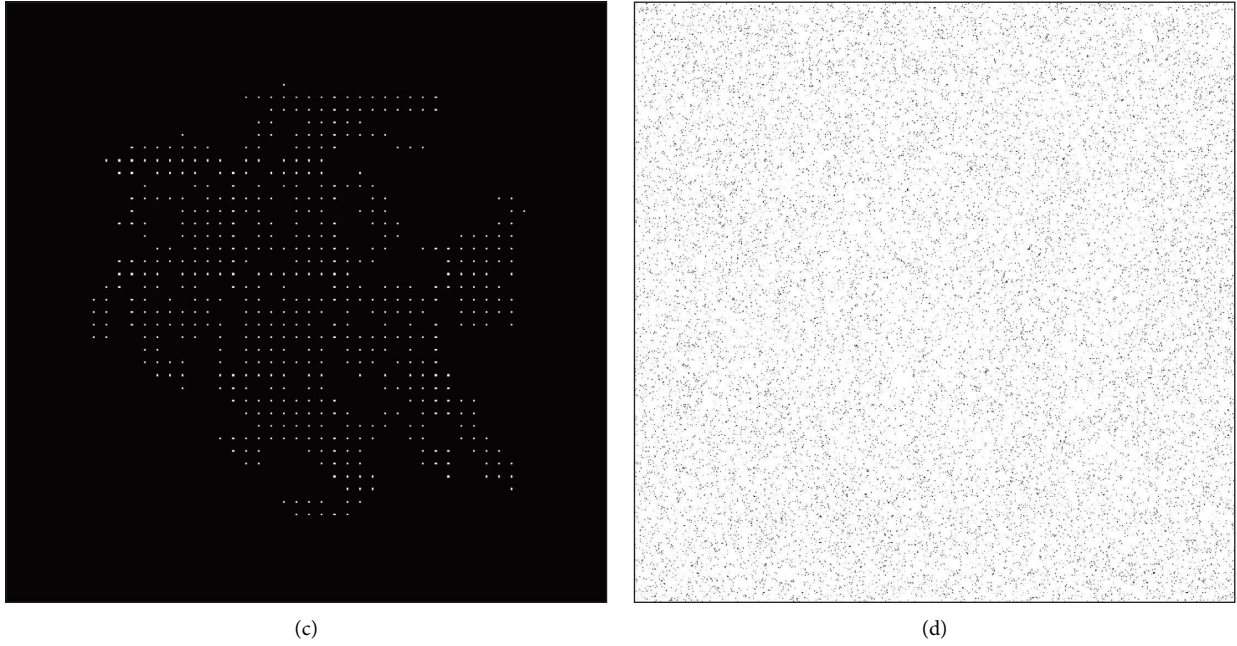
Figure 13: Continued.

(c)

(d)

FIGURE 13: The Gaussian white noise added to the initial dot skeleton partially or fully destroys the decoded image. Initial dot skeletons with the added Gaussian noise (zero mean and the variance equal to 10^{-5} and 10^{-2}) are depicted in parts (a) and (c). The decoded images are shown in panels (b) and (d) accordingly.
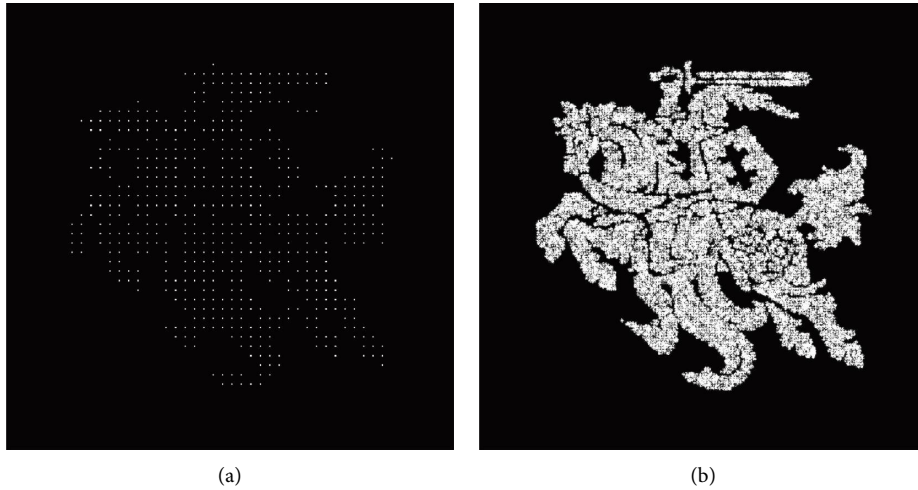

(a)

(b)

FIGURE 14: The secret information is encoded in linearly transformed secret image (part (a)). If the dot skeleton is multiplied by a constant value, the secret image will be decoded correctly (part (b)).

initial perturbations induced at those points would be able to interact during the evolution of the model.

It is important to observe that the perturbation at the dot skeleton point does not need to be large (it is below the noise level in [65]). Also, the excitable media of the model should guarantee that the initial perturbation in a single pixel does generate the effect of finite-time divergence in the surrounding of that pixel [55]. And the interaction between zones of finite-time divergence is responsible for the generation of the secret image. Clearly, the construction of the dot skeleton representation of the secret image is closely

related to the carrying capacity of the scheme and the parameters of the governing evolutionary model [55]. The construction strategy of the dot skeleton representation in this paper is directly incorporated from [55].

4.4. The Robustness of the Proposed Scheme against Partial Image Destruction Attacks. Without loss or generality, let us consider a hyper CML with the nodal dimension equal to 2. Also, a higher resolution of the proposed scheme is considered ($N_x = N_y = 1000$). The evolution of the single pattern (the Coat of Arms) is presented in Figure 10; the

coupling parameter ε is set to 0.13; the parameter of the logistic map a is set to 3.59. The hyper CML is perturbed at the nodes corresponding to the dot skeleton representation of the secret image (the distance between two adjacent pixels is set to 5). The perturbation is executed by setting the initial conditions of $\mu_1^{(0)}(i, j)$ to 1 at the nodes corresponding to the dot skeleton representation of the Coat of Arms. The initial values of $\lambda_0^{(0)}(i, j)$ are set as random numbers uniformly distributed in the interval $(0, 1)$. Patterns produced after 10, 20, 50, 100, 200, 300, 400, and 600 time-steps are depicted in Figure 10. The best reconstruction of the secret image is reached after 92 iterations.

The robustness against cropping attacks is an important feature of any image hiding scheme. The proposed scheme can resist a partial destruction of the dot skeleton. The area of the cropped square (marked in red in Figure 11(a)) is 4% of all 1000×1000 pixels in the dot skeleton representation of the Coat of Arms. The evolved pattern in the hyper CML is shown in Figure 11(b) (all parameters remain the same as in Figure 10).

The resistance to noise attack by adding 1% of the 'salt and pepper' type noise to the dot skeleton image (Figure 12(a)) is depicted in Figure 12(b). It can be seen that the corruption of 25% of pixels in the dot skeleton representation (Figure 12(c)) results into a complete destruction of the decoded image (Figure 12(d)).

The resistance of the proposed scheme to the Gaussian noise attack (zero mean and variance equal to 10^{-5}, Figure 13(a)) is illustrated in Figure 13(b). Note that the Gaussian noise with variance equal to 10^{-2} (Figure 13(c)) completely prevents the interpretation of the decoded image (Figure 13(d)).

The linear transformation of the perturbated values of the dot skeleton does not change the decoded image. The dot skeleton values multiplied by a constant 0.3 are depicted in Figure 14(a). The decoded image is presented in Figure 14(b).

5. Concluding Remarks

The image hiding scheme in the coupled map lattice of nilpotent matrices is presented in this paper. Complex nonsymmetric interactions between the auxiliary parameters governing the evolution of the iterative scheme enable hiding multiple secret images in a single two-dimensional lattice.

All computational experiments are performed with the proposed hyper CML. It is well known that the change in precision can change the properties of numerically investigated chaotic systems [66]. All computations in this paper are performed using standard double-precision floating-point numbers in MATLAB. The possible extension of the presented scheme to higher-dimensional matrices (a hyper CML of n-dimensional matrices) is completely straight-forward, and the carrying capacity of such scheme is $n - 1$ different secret images. As noted previously, a definite advantage of the proposed scheme is that the decoding of the secret does not require the computation of any different images.

Though this paper does present a novel scheme for hiding multiple images, the main focus is on the new type of CML. The introduction of the hyper CML is one of the main contributions of this paper. This is due to the properties of the hyper CML that the proposed scheme is simply possible.

The proposed image hiding scheme is implemented using the scalar mapping function of the logistic map. Higher-order derivatives of the logistic mapping function vanish because it is a second-order polynomial. The structure of coupled iterative maps represented by (14) becomes simpler compared to the general case in (12). Also, all perturbations at the nodes of the dot skeleton representation of the secret images are performed in terms of the auxiliary parameters. In other words, the parameter of the logistic map remains fixed during the whole computational process ($a = 3.59$). It is well-known that the logistic map has stability islands in its region of chaotic behavior (Figure 1(a)). However, since the parameter of the logistic map is fixed, the existence of stability islands cannot be considered as a weakness of the proposed information hiding scheme.

The situation would become completely different if a more complex scalar mapping function is used instead. For example, higher order derivatives of the mapping function of the fractional logistic map [67], or the intertwined logistic map [68] would not vanish. Then, the governing equations in (16) and relationships between auxiliary parameters would be much more complex compared to the schematic diagram depicted in Figure 3. That could open new possibilities for designing more complex image hiding schemes based on hyper CML. For example, the fractional logistic map would eliminate the existence of degenerate initial conditions which yield periodic orbits of the logistic map [67], and the intertwined logistic map would eliminate the nonuniformity of the distribution of the logistic map [68]. Such schemes do remain a definite objective of future research.

Data Availability

The datasets generated during and/or analyzed during the current study are available from the corresponding author on reasonable request.

Conflicts of Interest

The authors declare that there are no conflicts of interest regarding the publication of this paper.

Acknowledgments

References

[1] K. Kaneko, "Period-doubling of kink-antikink patterns, quasiperiodicity in antiferro-like structures and spatial

intermittency in coupled logistic lattice: towards a prelude of a "field theory of chaos," *Progress of Theoretical Physics*, vol. 72, no. 3, pp. 480–486, 1984.

[2] K. Kaneko, "Spatiotemporal intermittency in coupled map lattices," *Progress of Theoretical Physics*, vol. 74, no. 5, pp. 1033–1044, 1985.

[3] K. Kaneko, "Spatiotemporal chaos in one- and two-dimensional coupled map lattices," *Physica D: Nonlinear Phenomena*, vol. 37, no. 1-3, pp. 60–82, 1989.

[4] A. Zaghloul, T. Zhang, H. Hou, M. Amin, A. A. Abd El-Latif, and M. S. Abd El-Wahab, "A block encryption scheme for secure still visual data based on one-way coupled map lattice," *International Journal of Security and Its Applications*, vol. 8, no. 4, pp. 89–100, 2014.

[5] H. Movafegh Ghadirli, A. Nodehi, and R. Enayatifar, "Color image DNA encryption using mRNA properties and non-adjacent coupled map lattices," *Multimedia Tools and Applications*, vol. 80, no. 6, pp. 8445–8469, 2021.

[6] X. Wang, H. Zhao, and M. Wang, "A new image encryption algorithm with nonlinear-diffusion based on multiple coupled map lattices," *Optics & Laser Technology*, vol. 115, pp. 42–57, 2019.

[7] Y.-Q. Zhang, Y. He, P. Li, and X.-Y. Wang, "A new color image encryption scheme based on 2DNLCML system and genetic operations," *Optics and Lasers in Engineering*, vol. 128, Article ID 106040, 2020.

[8] W. Xingyuan, F. Le, W. Shibing, C. Zhang, and Z. Yingqian, "Spatiotemporal chaos in coupled logistic map lattice with dynamic coupling coefficient and its application in image encryption," *IEEE Access*, vol. 6, pp. 39705–39724, 2018.

[9] Y. Dong, G. Zhao, Y. Ma, Z. Pan, and R. Wu, "A novel image encryption scheme based on pseudo-random coupled map lattices with hybrid elementary cellular automata," *Information Sciences*, vol. 593, pp. 121–154, 2022.

[10] X. Wang, X. Qin, and C. Liu, "Color image encryption algorithm based on customized globally coupled map lattices," *Multimedia Tools and Applications*, vol. 78, no. 5, pp. 6191–6209, 2019.

[11] X. Lv, X. Liao, and B. Yang, "A novel pseudo-random number generator from coupled map lattice with time-varying delay," *Nonlinear Dynamics*, vol. 94, no. 1, pp. 325–341, 2018.

[12] G. Lu, R. Smidtaite, Z. Navickas, and M. Ragulskis, "The effect of explosive divergence in a coupled map lattice of matrices," *Chaos, Solitons & Fractals*, vol. 113, pp. 308–313, 2018.

[13] R. Smidtaite, G. Lu, and M. Ragulskis, "Image entropy for the identification of chimera states of spatiotemporal divergence in complex coupled maps of matrices," *Entropy*, vol. 21, no. 5, p. 523, 2019.

[14] N. Aarthie and R. Amirtharajan, "Image encryption: an information security perceptive," *Journal of Artificial Intelligence*, vol. 7, no. 3, p. 123, 2014.

[15] M. Kaur, S. Singh, and M. Kaur, "Computational image encryption techniques: a comprehensive review," *Mathematical Problems in Engineering*, vol. 2021, Article ID 5012496, 17 pages, 2021.

[16] Y. Xie, J. Yu, S. Guo, Q. Ding, and E. Wang, "Image encryption scheme with compressed sensing based on new three-dimensional chaotic system," *Entropy*, vol. 21, no. 9, p. 819, 2019.

[17] A. Jolfaei, A. Matinfar, and A. Mirghadri, "Preserving the confidentiality of digital images using a chaotic encryption scheme," *International Journal of Electronic Security and Digital Forensics*, vol. 7, no. 3, pp. 258–277, 2015.

[18] U. Zia, M. McCartney, B. Scotney et al., "Survey on image encryption techniques using chaotic maps in spatial, transform and spatiotemporal domains," *International Journal of Information Security*, vol. 21, no. 4, pp. 917–935, 2022.

[19] J. A. Alzubi, O. A. Alzubi, G. Suseendran, and D. Akila, "A novel chaotic map encryption methodology for image cryptography and secret communication with steganography," *International Journal of Recent Technology and Engineering*, vol. 8, no. 1, pp. 1122–1128, 2019.

[20] A. H. Khaleel and I. Q. Abduljaleel, "Chaotic image cryptography systems: a review," *Samarra Journal of Pure and Applied Science*, vol. 3, no. 2, pp. 129–143, 2021.

[21] M. Begum and M. S. Uddin, "Digital image watermarking techniques: a review," *Information*, vol. 11, no. 2, p. 110, 2020.

[22] D. K. Mahto and A. K. Singh, "A survey of color image watermarking: state-of-the-art and research directions," *Computers & Electrical Engineering*, vol. 93, Article ID 107255, 2021.

[23] S.-P. Lu, R. Wang, T. Zhong, and P. L. Rosin, "Large-capacity image steganography based on invertible neural networks," in *Proceedings of the IEEE/CVF Conference on Computer Vision and Pattern Recognition*, pp. 10816–10825, Nashville, TN, USA, June 2021.

[24] O. Y. Abdulhammed, "A novel approach of steganography by using strong edge detection and chaos theory," *Multimedia Tools and Applications*, vol. 81, no. 13, pp. 17875–17888, 2022.

[25] N. Kanzariya, D. Jadhav, G. Lakhani, U. Chauchan, and L. Gagani, "Coverless information hiding: a review," in *Proceedings of International Conference on Computational Intelligence*, R. Tiwari, M. F. Pavone, and R. Ravindranathan Nair, Eds., pp. 109–135, Springer Nature Singapore, Singapore, 2023.

[26] Z. Zhou, H. Sun, R. Harit, X. Chen, and X. Sun, "Coverless image steganography without embedding," in *Cloud Computing and Security: First International Conference, ICCCS 2015*, vol. 1, pp. 123–132, Springer, Berlin, Germany, 2015.

[27] C. Yu, D. Hu, S. Zheng, W. Jiang, M. Li, and Z. Zhao, "An improved steganography without embedding based on attention GAN," *Peer-to-Peer Networking and Applications*, vol. 14, no. 3, pp. 1446–1457, 2021.

[28] Q. Li, X. Wang, X. Wang, B. Ma, C. Wang, and Y. Shi, "An encrypted coverless information hiding method based on generative models," *Information Sciences*, vol. 553, pp. 19–30, 2021.

[29] Y. Long, Y. Liu, Y. Zhang, X. Ba, and J. Qin, "Coverless information hiding method based on web text," *IEEE Access*, vol. 7, pp. 31926–31933, 2019.

[30] J. Fridrich, "Image encryption based on chaotic maps," in *Proceedings of the 1997 IEEE international conference on systems, man, and cybernetics Computational cybernetics and simulation*, vol. 2, pp. 1105–1110, IEEE, Madrid, Spain, June 1997.

[31] T. Gao and Z. Chen, "A new image encryption algorithm based on hyper-chaos," *Physics Letters A*, vol. 372, no. 4, pp. 394–400, 2008.

[32] X. Wang, J. Zhao, and H. Liu, "A new image encryption algorithm based on chaos," *Optics Communications*, vol. 285, no. 5, pp. 562–566, 2012.

[33] P. R. Sankpal and P. A. Vijaya, "Image encryption using chaotic maps: a survey," in *Proceedings of the 2014 5th international conference on signal and image processing*, pp. 102–107, IEEE, Bangalore, India, January 2014.

[34] N. K. Pareek, V. Patidar, and K. K. Sud, "Image encryption using chaotic logistic map," *Image and Vision Computing*, vol. 24, no. 9, pp. 926–934, 2006.

[35] W. Liu, K. Sun, and C. Zhu, "A fast image encryption algorithm based on chaotic map," *Optics and Lasers in Engineering*, vol. 84, pp. 26–36, 2016.

[36] J. Zhao, S. Wang, Y. Chang, and X. Li, "A novel image encryption scheme based on an improper fractional-order chaotic system," *Nonlinear Dynamics*, vol. 80, no. 4, pp. 1721–1729, 2015.

[37] B. Norouzi and S. Mirzakuchaki, "Breaking a novel image encryption scheme based on an improper fractional order chaotic system," *Multimedia Tools and Applications*, vol. 76, no. 2, pp. 1817–1826, 2017.

[38] G. Gu and J. Ling, "A fast image encryption method by using chaotic 3D cat maps," *Optik*, vol. 125, no. 17, pp. 4700–4705, 2014.

[39] M. A. Murillo-Escobar, C. Cruz-Hernández, F. Abundiz-Pérez, R. M. López-Gutiérrez, and O. R. Acosta Del Campo, "A RGB image encryption algorithm based on total plain image characteristics and chaos," *Signal Processing*, vol. 109, pp. 119–131, 2015.

[40] C. Han, "An image encryption algorithm based on modified logistic chaotic map," *Optik*, vol. 181, pp. 779–785, 2019.

[41] J. Oravec, L. Ovsenik, and J. Papaj, "An image encryption algorithm using logistic map with plaintext-related parameter values," *Entropy*, vol. 23, no. 11, p. 1373, 2021.

[42] C. Li, G. Luo, K. Qin, and C. Li, "An image encryption scheme based on chaotic tent map," *Nonlinear Dynamics*, vol. 87, no. 1, pp. 127–133, 2017.

[43] C. Zhu and K. Sun, "Cryptanalyzing and improving a novel color image encryption algorithm using RT-enhanced chaotic tent maps," *IEEE Access*, vol. 6, pp. 18759–18770, 2018.

[44] G. Ye and K.-W. Wong, "An efficient chaotic image encryption algorithm based on a generalized Arnold map," *Nonlinear Dynamics*, vol. 69, no. 4, pp. 2079–2087, 2012.

[45] K. C. Jithin and S. Sankar, "Colour image encryption algorithm combining Arnold map, DNA sequence operation, and a Mandelbrot set," *Journal of Information Security and Applications*, vol. 50, Article ID 102428, 2020.

[46] D. Chattopadhyay, M. K. Mandal, and D. Nandi, "Symmetric key chaotic image encryption using circle map," *Indian Journal of Science and Technology*, vol. 4, no. 5, pp. 593–599, 2011.

[47] Z. Fan, T. Xiao-Jian, F. Wen-Hua, L. Xue-Yan, and G. Bo, "Image encryption based on Henon map," *Journal of Beijing University of Posts and Telecommunications*, vol. 31, no. 1, p. 66, 2008.

[48] N. Jiang, X. Dong, H. Hu, Z. Ji, and W. Zhang, "Quantum image encryption based on Henon mapping," *International Journal of Theoretical Physics*, vol. 58, no. 3, pp. 979–991, 2019.

[49] F. Han, X. Yu, and S. Han, "Improved baker map for image encryption," in *Proceedings of the 2006 1st International Symposium on Systems and Control in Aerospace and Astronautics*, p. 4, IEEE, Harbin, China, January 2006.

[50] L. Liu and S. Miao, "An image encryption algorithm based on Baker map with varying parameter," *Multimedia Tools and Applications*, vol. 76, no. 15, pp. 16511–16527, 2017.

[51] S. Wang, J. Kuang, J. Li, Y. Luo, H. Lu, and G. Hu, "Chaos-based secure communications in a large community," *Physical Review*, vol. 66, no. 6, Article ID 065202, Dec 2002.

[52] C.-Y. Song, Y.-L. Qiao, and X.-Z. Zhang, "An image encryption scheme based on new spatiotemporal chaos," *Optik –*

[52] *International Journal for Light and Electron Optics*, vol. 124, no. 18, pp. 3329–3334, 2013.

[53] S. Lian, "Efficient image or video encryption based on spatiotemporal chaos system," *Chaos, Solitons & Fractals*, vol. 40, no. 5, pp. 2509–2519, 2009.

[54] X. Wang, N. Guan, H. Zhao, S. Wang, and Y. Zhang, "A new image encryption scheme based on coupling map lattices with mixed multichaos," *Scientific Reports*, vol. 10, no. 1, p. 9784, 2020.

[55] G. Lu, R. Smidtaite, D. Howard, and M. Ragulskis, "An image hiding scheme in a 2-dimensional coupled map lattice of matrices," *Chaos, Solitons & Fractals*, vol. 124, pp. 78–85, 2019.

[56] R. Smidtaite, Z. Navickas, and M. Ragulskis, "Clocking divergence of iterative maps of matrices," *Communications in Nonlinear Science and Numerical Simulation*, vol. 95, Article ID 105589, 2021.

[57] X. Liu, Z. Ma, Z. Chen et al., "Hiding multiple images into a single image via joint compressive autoencoders," *Pattern Recognition*, vol. 131, Article ID 108842, 2022.

[58] A. Jain, "A secured steganography technique for hiding multiple images in an image using least significant bit algorithm and Arnold transformation," in *International Conference on Intelligent Data Communication Technologies and Internet of Things*, , pp. 373–380, Springer, 2019.

[59] Z. Guan, J. Jing, X. Deng et al., "DeepMIH: deep invertible network for multiple image hiding," *IEEE Transactions on Pattern Analysis and Machine Intelligence*, vol. 45, no. 1, pp. 372–390, 2023.

[60] L. Tao, X. Liang, B. Hu, and L. Han, "Compound encryption of multiple images by utilizing a novel chaos and nonlinear transform," *Neural Computing & Applications*, vol. 3, 2022.

[61] Z. Navickas, R. Smidtaite, A. Vainoras, and M. Ragulskis, "The logistic map of matrices," *Discrete & Continuous Dynamical Systems-B*, vol. 16, no. 3, pp. 927–944, 2011.

[62] Z. Navickas, M. Ragulskis, A. Vainoras, and R. Smidtaite, "The explosive divergence in iterative maps of matrices," *Communications in Nonlinear Science and Numerical Simulation*, vol. 17, no. 11, pp. 4430–4438, 2012.

[63] R. May, "Simple mathematical models with very complicated dynamics," *Nature*, vol. 261, no. 5560, pp. 459–467, 1976.

[64] R. C. Hilborn, *Chaos and Nonlinear Dynamics: An Introduction for Scientists and Engineers*, Oxford University Press on Demand, Oxford, UK, 2000.

[65] L. Saunoriene and M. Ragulskis, "Secure steganographic communication algorithm based on self-organizing patterns," *Physical Review*, vol. 84, no. 5, Article ID 056213, 2011.

[66] D. Arroyo, F. Hernandez, and A. B. Orúe, "Cryptanalysis of a classical chaos-based cryptosystem with some quantum cryptography features," *International Journal of Bifurcation and Chaos*, vol. 27, no. 1, Article ID 1750004, 2017.

[67] D. Petkevičiūtė-Gerlach, I. Timofejeva, and M. Ragulskis, "Clocking convergence of the fractional difference logistic map," *Nonlinear Dynamics*, vol. 100, no. 4, pp. 3925–3935, 2020.

[68] X. Wang and D. Luan, "A novel image encryption algorithm using chaos and reversible cellular automata," *Communications in Nonlinear Science and Numerical Simulation*, vol. 18, no. 11, pp. 3075–3085, 2013.